37
-/3/80

DR. 1205

SAN-2207-T4

THIN FILM POLYCRYSTALLINE SILICON SOLAR CELLS

Final Report, September 25, 1978—September 25, 1979

By
K. R. Sarma
M. J. Rice
R. Legge
R. W. Gurtler
W. C. Ramsey

December 1, 1979

Work Performed Under Contract No. ET-78-C-03-2207

Motorola, Inc.
Solar Energy Department
Phoenix, Arizona

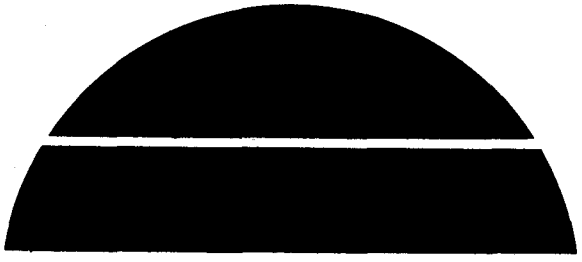

U.S. Department of Energy

Solar Energy

SAN-2207-T4
Distribution Category UC-63e

THIN FILM POLYCRYSTALLINE SILICON SOLAR CELLS

FINAL REPORT

25 SEPTEMBER 1978 - 25 SEPTEMBER 1979

PREPARED FOR

UNITED STATES DEPARTMENT OF ENERGY

DIVISION OF SOLAR TECHNOLOGY

600 E. STREET, N.W.

WASHINGTON, D.C. 20545

PREPARED BY

K.R. SARMA, M.J. RICE, R. LEGGE, R.W. GURTLER, W.C. RAMSEY

OF

MOTOROLA, INC.
SOLAR ENERGY DEPARTMENT
5005 EAST McDOWELL ROAD
PHOENIX, ARIZONA 85008

DECEMBER 1, 1979

MOTOROLA PROJECT NO. 2361

DOE CONTRACT NO. ET-78-C-03-2207

PREFACE

This Annual (Final) Report, covering the period September 25, 1978 to Sepbember 25, 1979, was prepared by the Solar Energy R&D Department, I. A. Lesk, Manager, Manager, Motorola Inc., Phoenix, Arizona 85008. The report describes the work performed under DOE Contract No. ET-78-C-03-2207. K. R. Sarma is the principal investigator. Others who participated in this program are R. W. Gurtler, M. J. Rice, R. Legge, B. Sopori, and W. C. Ramsey.

ABSTRACT

The main objective of this research program was to develop a new method of depositing thin polycrystalline silicon films, utilizing an Energy Beam, for producing solar cells capable of meeting the long range economic and performance objectives of D.O.E.'s National Photovoltaics program. The main task was divided into the following four sub-tasks: (1) investigation of the Energy Beam as a means for efficient, high-rate deposition of polysilicon films; (2) development of temporary, reuseable substrates for polysilicon deposition; (3) subsequent grain enhancement of self-supporting thin silicon films through laser recrystallization; and (4) demonstration of at least 10% efficient solar cells fabricated on these grain enhanced silicon films.

Molybdenum TESS substrates were characterized as they are recycled by a variety of analytical techniques such as SEM, DEKTAK, X-ray diffraction and AES. Two interfacial layers, $MoSi_2$ and Mo_5Si_3, were found to form between the Mo substrate and the Si film. The $MoSi_2$ layer thickness was found to increase with the number of deposition cycles (a function of time and temperature) and it was found to be controlled by the diffusion of Si through the $MoSi_2$ lattice. However, the Mo_5Si_3 layer thickness was found to remain nearly constant at 2 - 3 μm. (i.e. it is growing at the same rate as it is being consumed). Shear separation occurs in the deposited silicon film very close (~100Å) to the $MoSi_2$-Si interface. For reliable shear separation to occur, a high ΔT (difference between the deposition temperature and the final temperature) was not found to be necessary. A time-temperature combination was found to be important. High temperature growth for a short time, low temperature growth followed by a short high temperature anneal, or low temperature growth followed by a long low temperature anneal, were found to result in reliable shear separation. Thin films of

SiO_2, Si_3N_4 and Al_2O_3 were investigated for their effectiveness as diffusion barriers (for preventing $MoSi_2$ layer growth) and it was found that SiO_2 is ideal for this purpose. Using an SiO_2 diffusion barrier, a composite TESS substrate structure was developed; this shows promise for substantially improving the substrate recyclability. Also, various novel substrates such as thin Mo coated graphite, and Mo coated Al_2O_3 have been investigated and shear separation has been observed from both Mo coated graphite and Al_2O_3 substrates. The continued reliability of shear separation from Mo substrates appears to be affected by accidental oxidation of the $MoSi_2$ separation layer (forming an SiO_2 surface layer) and also by progressive roughening of the $MoSi_2$ layer with repeated use.

Parameters of the horizontal and vertical EBD systems were optimized and large area (up to 1½" wide and 18" long) self-supporting p-type polycrystalline silicon ribbons have been produced using these system with $SiHCl_3$ as the silicon source gas. Deposition efficiency was found to decrease with increasing $\frac{Cl}{H}$ ratio in the reactant gas stream. Average EBD efficiencies experimentally observed were higher by a few percent (0 to 5%) for $\frac{Cl}{H}$ ratios <0.12, and lower by a few percent for $\frac{Cl}{H}$ >0.12, compared to a theoretical maximum (equilibrium) efficiency obtainable by a conventional CVD process. Also EBD efficiency was found to decrease with increasing total reactant flow rate. The efficiency in the vertical EBD system was lower than in the horizontal apparatus by up to 7%. This is believed to result from more of the gas phase nucleated silicon particles getting exhausted from the deposition system (rather than being incorporated into the growing silicon ribbon) in the vertical configuration compared to a horizontal design. Some of the silicon ribbons produced in the batch EBD systems contained whiskers and nodules. A major mechanism for nodule and whisker growth in EBD was found to be through the landing of large silicon particles (gas phase nucleated) on the growing silicon ribbon.

When the particle lands with a favorable orientation, whisker growth occurs by re-entrant twin mechanism; otherwise it will result in nodule formation.

A rotating electrode nozzle has been developed to eliminate the deleterious effects of beam arcing. Using this nozzle, the plasma beam was successfully rotated during silicon deposition, thus uniformly heating the substrates. A continual EBD system was designed (using the rotating nozzle) and fabricated. Initial testing of this system was completed, and initial problems with the substrate translation mechanism and dynamic seals were overcome. With a CVD mode of operation, several 2" x 12" silicon ribbons were produced using this system in a single run.

EBD silicon ribbons, after RTR laser recrystallization, were found to contain very few grain boundaries, but many twin boundaries and dislocations. Several crystal regions were up to several mm wide and several cm long. A new grain enhancement procedure named "rigid edge" growth has been used for efficiently grain enhancing most of the area of finite length microcrystalline EBD silicon ribbons. While some experiments were performed to determine the effects of resistivity, most of the experiments were performed with the ribbons doped to have a resistivity of about 1 Ω-cm. Minority carrier diffusion length in as-recrystallized EBD ribbons, as measured by the SPV technique, was in the range of 5 - 20 μm. A double-sided phosphorus diffusion gettering procedure was developed for improving diffusion length; by this gettering procedure, diffusion length was found to improve up to 100 μm. Solar cells, 1 cm x 2 cm in area, have been fabricated using a simple processing sequence. This has resulted in solar cells with efficiencies of up to 10.1%, V_{OC} of 0.54V, J_{SC} of 29.5 mA/cm^2 and FF of 63% under simulated AM1 illumination for ribbons with 1 Ω-cm resistivity. The efficiencies observed with 0.3 Ω-cm resistivity ribbons were in the range of 7.5 - 8.0%. The short circuit current in these cells was about 10 - 20% lower than in the 1 Ω-cm base

resistivity cells. Also these cells were found to suffer from localized shunting problems as indicated by a significant decrease in V_{OC} after metallization. Some experiments were also conducted to determine the effects of substrate temperature during Energy Beam Deposition on solar cell efficiency parameters. Contrary to expectation, diffusion length in the grain enhanced ribbon was found to decrease (e.g. from 20 μm to 9 μm) as the substrate temperature decreased (from 1125^{o}C to 1050^{o}C).

TABLE OF CONTENTS

LIST OF FIGURES

LIST OF TABLES

1.0 INTRODUCTION

The objectives of this research program are: (1) investigation of the Energy Beam as a means for efficient, high-rate deposition of polysilicon films; (2) development of temporary, reuseable substrates for polysilicon deposition; (3) subsequent grain enhancement of the thin silicon films through laser recrystallization; and (4) demonstration of at least 10% efficient solar cells fabricated on these grain enhanced silicon films.

During this year, substantial progress has been made on all tasks of the program. Substrate system experiments are discussed in Chapter 2. These studies include characterization of the Mo TESS substrates for shear separation mechanism, substrate temperature requirements, development of diffusion barriers, development of a composite TESS substrate, novel substrates, and continued reliability of shear separation from Mo substrates. Chapter 3 describes the Energy Beam Deposition (EBD) experiments. In this chapter, batch EBD systems and parametric studies using these systems are discussed. Deposit characterization studies, plasma geometry studies, and the first version of a continual EBD system are also included. Chapter 4 discusses grain size enhancement and characterization studies. Solar cell fabrication and evaluation studies are described in Chapter 5. These studies include determining the effects of base resistivity, substrate temperature during Energy Beam deposition, and gettering cycles, on solar cell efficiency parameters. Conclusions and recommendations are presented in Chapter 6.

2.0 SUBSTRATE SYSTEM STUDIES

Substrate studies were carried out in conventional induction-heated CVD systems for the sake of convenience. Selected experiments were repeated in an energy beam system, each experiment designed to verify results obtained in the induction-heated system. Mixtures of H_2-$SiCl_4$ or H_2-SiH_4 were used as process gases. These studies were aimed at gaining an increased understanding of the reactions taking place at the silicon-substrate interface, and of the effect of selected substrate coatings on shear separation or their effectiveness as diffusion barriers. All important substrate system studies are summarized in Tables 1 - 3 under the titles "Mo substrate experiments", "Composite TESS substrate experiments", and "Novel substrate experiments" and are described in detail below.

2.1 CHARACTERIZATION OF Mo TESS SUBSTRATES

Temperature requirements for thermal expansion shear separation (TESS) of a silicon film from a Mo substrate were examined. Substrate temperatures of 1000 - 1200°C were used for Si deposition, with shear separation invariably occurring when the deposition temperature was greater than 1100°C for a 1½ hour deposition. In order to test whether the amount of stress developed due to the expansion mismatch of silicon and molybdenum was the key variable, a simple test was performed. Since the ΔT in a normal shear separation was 1125°C (1150°-25° R.T.), a deposition was carried out at 1050°C and the substrate with the adherent silicon was immersed in liquid N_2 (ΔT = 1245°C). This did not result in shearing, indicating that for reliable separation to occur, formation of a $MoSi_2$ layer was necessary. The system Mo-Si can form three stable silicides $MoSi_2$, Mo_3Si and Mo_5Si_3. (1-5) Metallographic cross sections of Mo substrates always showed

TABLE 1

SUMMARY OF Mo SUBSTRATE EXPERIMENTS

NO.	EXPERIMENT	COMMENTS
1	Substrate Temperature	Temperature was varied from 1000 to 1200°C. Reliable shear separation occurred for temperature greater than 1000°C. ΔT between deposition temperature and final temperature shown not to be major factor. A time-temperature dependence was shown for shear separation to occur. A high temperature growth, or low temperature growth followed by a short high temperature anneal or long low temperature anneal, resulted in shear separation.
2	Substrate Surface Morphology	Surface finish was characterized with DEKTAK and SEM. Rough surface affected shear or first deposition with decreasing effect in succeeding depositions. After multiple depositions, surface grinding restored substrates to initial condition.
3	Identification of Silicide Phases	X-ray diffraction was used to identify $MoSi_2$ and Mo_5Si_3 layers on substrates.
4	Location of Shear	SEM with an energy dispersive x-ray unit and Auger electron spectroscopy were used in showing that shearing takes place in the silicon layer at or very near the $MoSi_2$-Si interface.
5	SiO_2 Diffusion Barriers	SiO_2 effective diffusion barrier. SEM revealed no $MoSi_2$ formation. No shear separation.
6	Si_3N_4 Barrier	Si_3N_4 does not act as barrier. $MoSi_2$ phase is formed and shear separation occurs. Promotes nucleation and improves ribbon quality.
7	Al_2O_3 Barrier	5000Å of Al_2O_3 does not act as barrier at 1150°C. $MoSi_2$ identified by X-ray diffraction.

TABLE 2

SUMMARY OF COMPOSITE TESS SUBSTRATE EXPERIMENTS

NO.	EXPERIMENT	COMMENTS
1.	Mo (thick)-SiO_2 (thin)-Mo (thin) Substrate	Sputtered or CVD Mo layer on top of CVD SiO_2 allows silicide formation and shearing to occur. Thick substrate is preserved by SiO_2 barrier.
2.	Mo-Si-SiO_2 Substrate	Si layer on substrate forms silicide and ribbon shears with SiO_2 barrier intact within silicon. After etching through SiO_2 barrier, no Mo detected by neutron activation analysis.

TABLE 3

SUMMARY OF NOVEL SUBSTRATE EXPERIMENTS

NO.	EXPERIMENT	COMMENTS
1.	Plasma sprayed Mo on Stainless Steel	Molybdenum layer too porous with silicon penetrating and forming silicides with stainless steel.
2.	Mo layer on Al_2O_3 substrate	Sputtered and CVD Mo layers 10,000Å. Silicon shears off leaving clean substrate. X-ray diffraction shows $MoSi_2$ and Mo_5Si_3 on the back of silicon ribbon.
3.	Mo layer on graphite	CVD Mo on Poco graphite; silicon shears off leaving clean graphite substrate. X-ray difrraction shows that the back of silicon ribbon does not contain any Mo.
4.	Powdery Si Coating	Powdery Si coatings on Mo, quartz, or alumina become densified during deposition. Ribbon adheres to quartz and alumina, and shears normally from Mo with silicide formation.

two silicide layers; a "thick" layer of $MoSi_2$ and a thin (2 - 3 μm) layer of a Mo-rich silicide (e.g. Figures 1,2). A sample was prepared for x-ray diffraction by etching away the Mo substrate in solution B (5% nitric acid, 80% phosphoric acid, 5% acetic acid, 10% water by volume, at 60°C) leaving self-supporting silicide layers. This enabled the sample to be mounted so that the x-ray beam was incident on the thin Mo-rich silicide layer. Table 4 shows the results of the x-ray diffraction compared with random powder samples for $MoSi_2$ and Mo_5Si_3. From the table it may be seen that all the observed reflections are attributable to the $MoSi_2$ and Mo_5Si_3 layers in the sample.

In addition to the x-ray diffraction, electron probe x-ray micro-analysis (EPMA) of the sample shown in Figure 2 indicated a 1:2 atom ratio for the thick silicide layer and approximately 1:1 ratio for the thin layer (which is more indicative of Mo_5Si_3 than Mo_3Si).

For reliable shearing to take place from Mo substrates, it was found that silicide formation was a prerequisite. Also, a time-temperature dependence was found. Equally effective to a high growth temperature (1150 - 1200°C) was a low growth temperature (1000 - 1050°C) followed by a 15 - 30 minute anneal at 1200°C. One Mo-substrate with a strongly adherent Si ribbon was annealed at 800°C. When cooled after 80 hours of annealing, approximately 3/4 of the ribbon sheared off. After 40 additional hours at 800°C, the remaining ribbon sheared. These data are strongly suggestive of a diffusion process being involved. In the formation of transition metal silicides, the diffusing species in the metal rich silicides is generally the metal while the diffusing species in the disilicides is silicon (1,5).

Figure 3 is a 2200X SEM of a silicon ribbon on the side that sheared from the substrate. An x-ray emission scan taken at the same time (Figure 4)

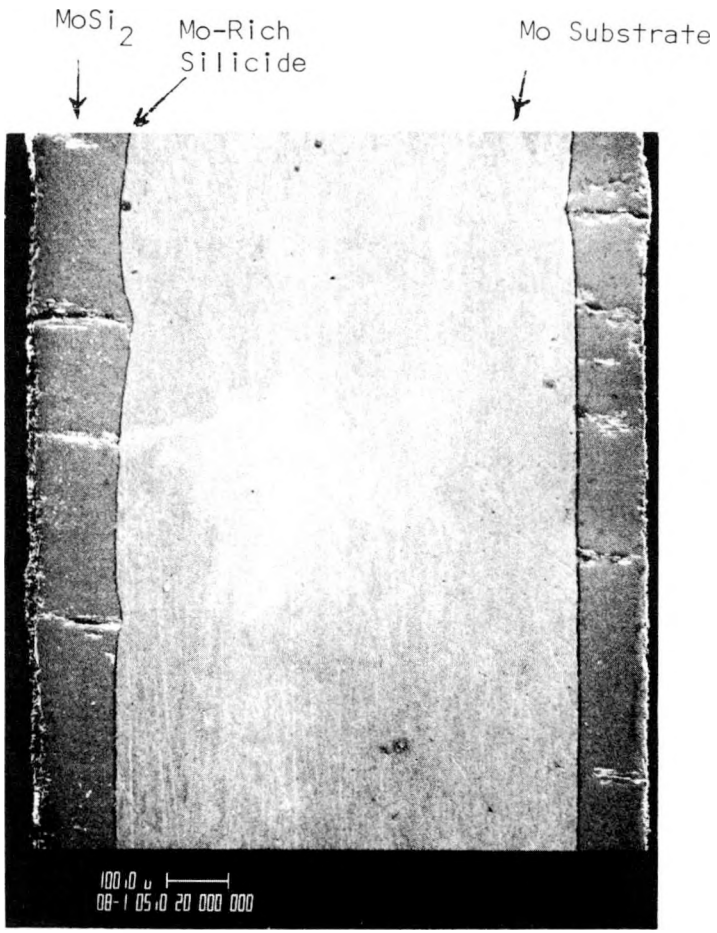

Figure 1. Cross-Sectional View of a Molybdenum Substrate Subjected to 8 Silicon Deposition Cycles

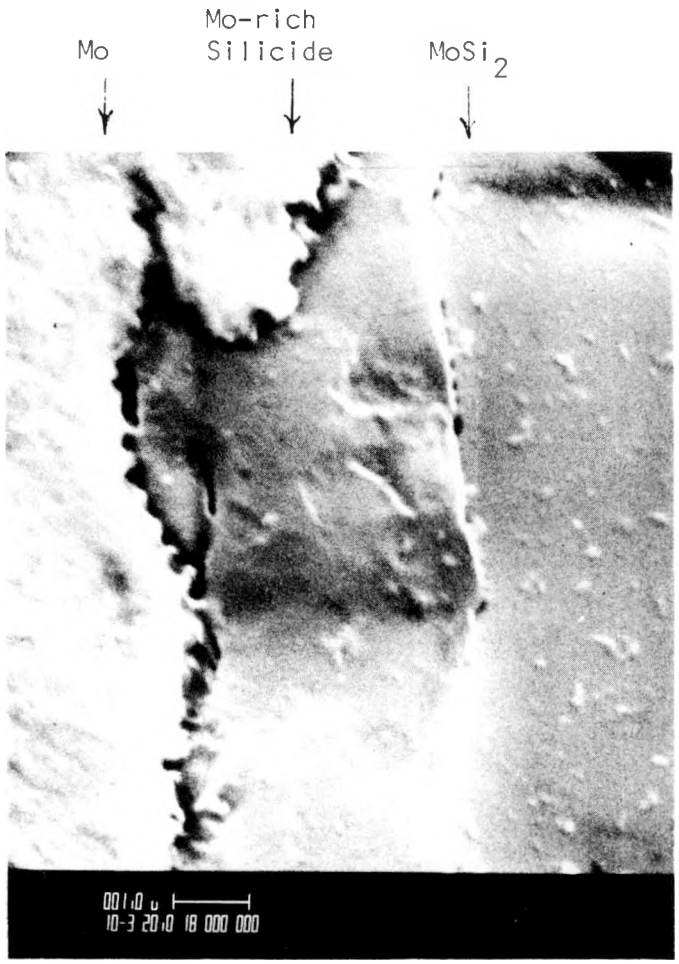

Figure 2. High Magnification SEM Photograph of the Sample Shown in Figure 1 Showing the Interface - Mo/Mo-rich-Silicide/$MoSi_2$

Figure 3. SEM Photograph of the Shear Separated Interface. Viewing Angle was 60°

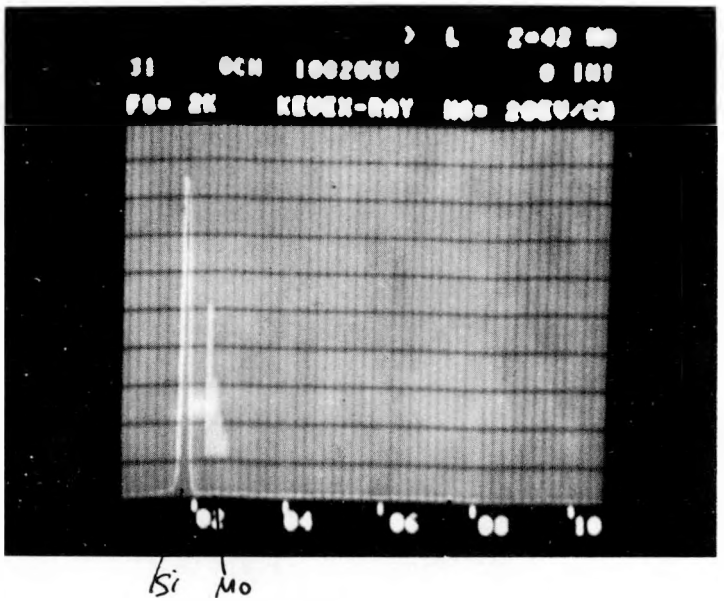

Figure 4. X-Ray Emission Scan in the SEM, Obtained from the Region of the Silicon Film Shown in Figure 3

TABLE 4

X-RAY DIFFRACTION PATTERNS OF Mo-SILICIDES

OBSERVED		$MoSi_2$ (6)			Mo_5Si_3 (7)		
d	I/I_o	d	I/I_o	h k l	d	I/I_o	h k l
3.92	12	3.92	45	002			
					3.23	20	211
					3.04	20	310
2.96	20	2.96	95	101			
2.45	100				2.443	10	002
					2.406	10	400
					2.342		110
2.26	88	2.26	70	110			
					2.174	20	202
					2.149	60	420
					2.102	50	411
2.02	8	2.02	100	103			
1.96	21	1.96	40	004,112	1.986	100	222
1.60	8	1.60	30	200			
					1.522	10	620
1.48	13	1.49	20	114,202	1.491	10	512
1.44	11				1.437	7	541
1.41	7	1.41	25	105,211			
					1.395	10	323
					1.376	10	631
					1.363	10	532
					1.339	20	602,413
1.31	7	1.308	16	006			
1.26	25	1.257	45	213			
		1.241	10	204	1.169	10	642

shows no indication of Mo, which indicates that shearing takes place in the silicon layer. Mayer (3) has suggested that when Si is the diffusing species in silicide formation, vacancies are created in the silicon layer at the interface; these vacancies may condense into voids, giving a possible explanation of why shearing takes place in the silicon film adjacent to the $MoSi_2$-Si interface.

Auger analysis has been used to characterize Mo substrates for compositional profiles through their thickness to obtain additional clues to the shear separation mechanism. Even though AES is not very accurate for quantitative compositional analysis, it is quite valuable when high depth resolution is required.

Figure 5 shows AES profiles near the shear separation interface. These concentrations were determined by the use of elemental sensitivity factors. Oxygen in Figure 5 can be from the native oxide present on the substrate surface. Thus this analysis indicates that the bulk concentration of the top (separation) layer is approximately MoSi which is in contradiction to the X-ray diffractometry results, which unequivocally indicated that it is $MoSi_2$. It should be noted that, in AES, the quantitative concentrations determined by elemental sensitivity factors are only ±30 to 50% accurate due to matrix variations which produce changes in escape depth and back scattering factors (8). Thus when we realize that silicon concentrations determined by Auger analysis are lower than actual and Mo concentrations are higher than actual, Figure 5 will indicate that, initially, there is an approximately 100Å thick silicon rich layer (perhaps pure silicon, if we ignore the presence of native oxide).
We have previously shown (9) by SIMS analysis that the back side of the separated silicon ribbon is almost pure silicon, but contains Mo at ppm levels. These results suggest that shear separation occurs in the silicon film very close to the $MoSi_2$-Si interface.

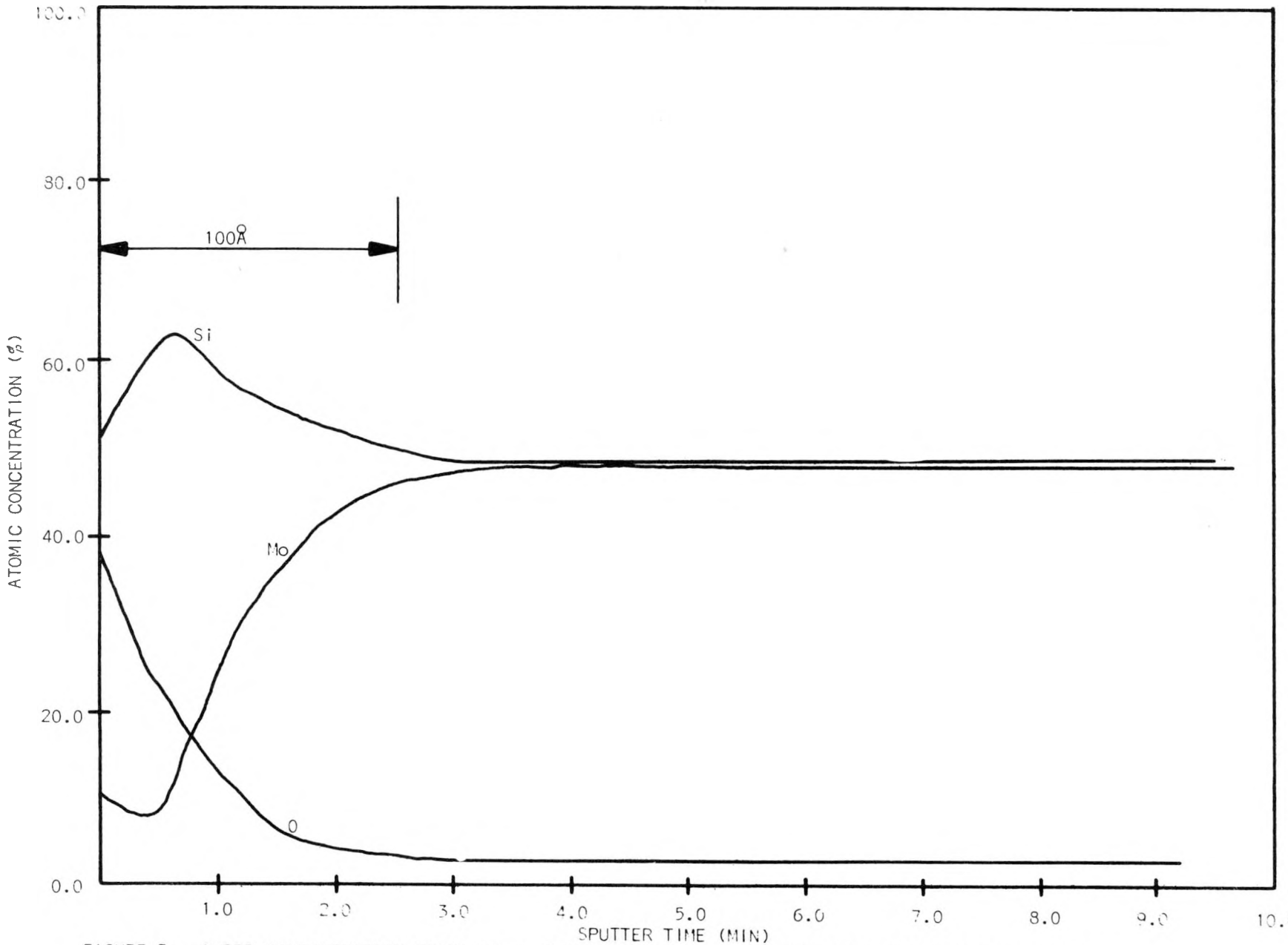

FIGURE 5: AUGER CONCENTRATION PROFILES IN THE Mo SUBSTRATE NEAR THE SHEAR SEPARATION INTERFACE.

The effect of surface roughness of the substrate on shearing was also investigated. Molybdenum sheet stock, as purchased for substrate material, is supplied in two surface finishes. For thickness below .030" a class 100 finish is available while the .040" thick sheets are available in class 300 finish. The surface roughness was tested with a Sloan Dektak for the two finishes. Figure 6 shows Dektak tracings for .040" thick substrates with a shiny finish. The second tracing in each figure is from a sample cleaned by etching in Solution B (5% nitric acid, 80% phosphoric acid, 5% acetic acid, 10% water by volume). Etching increases the height differences of the peaks and valleys. The third tracing in each figure shows the roughness after the substrates have been coated with 2000Å of Si_3N_4. This coating has been found to be beneficial in promoting nucleation of the silicon and in promoting more reliable shear separation.

SEM photographs were taken of the surfaces of .040" Mo substrates. Figure 8 shows the surface of an "as received" sheet of molybdenum. The direction of rolling is easily seen in the lower magnification, 500X photograph. Etching cleans the surface, but particularly noticeable is the delineation of grains as shown in Figure 9b. Coating the etched substrates with Si_3N_4 tends to round off the sharp edges as can be seen in Figure 10. In investigating substrate surfaces, several were polished to a mirror finish by lapping with 500 grit SiC, followed by polishing with 1 μm and 0.5 μm diamond paste. A polished substrate coated with Si_3N_4 is shown in Figure 11. The surface is noticeably smoother than unpolished substrates and is pockmarked with small pits. Silicon ribbons deposited on polished substrates are much smoother at the sheared surface for the first deposition. However, as the substrate is re-used, the separation surface of the silicon becomes rougher at each succeeding deposition.

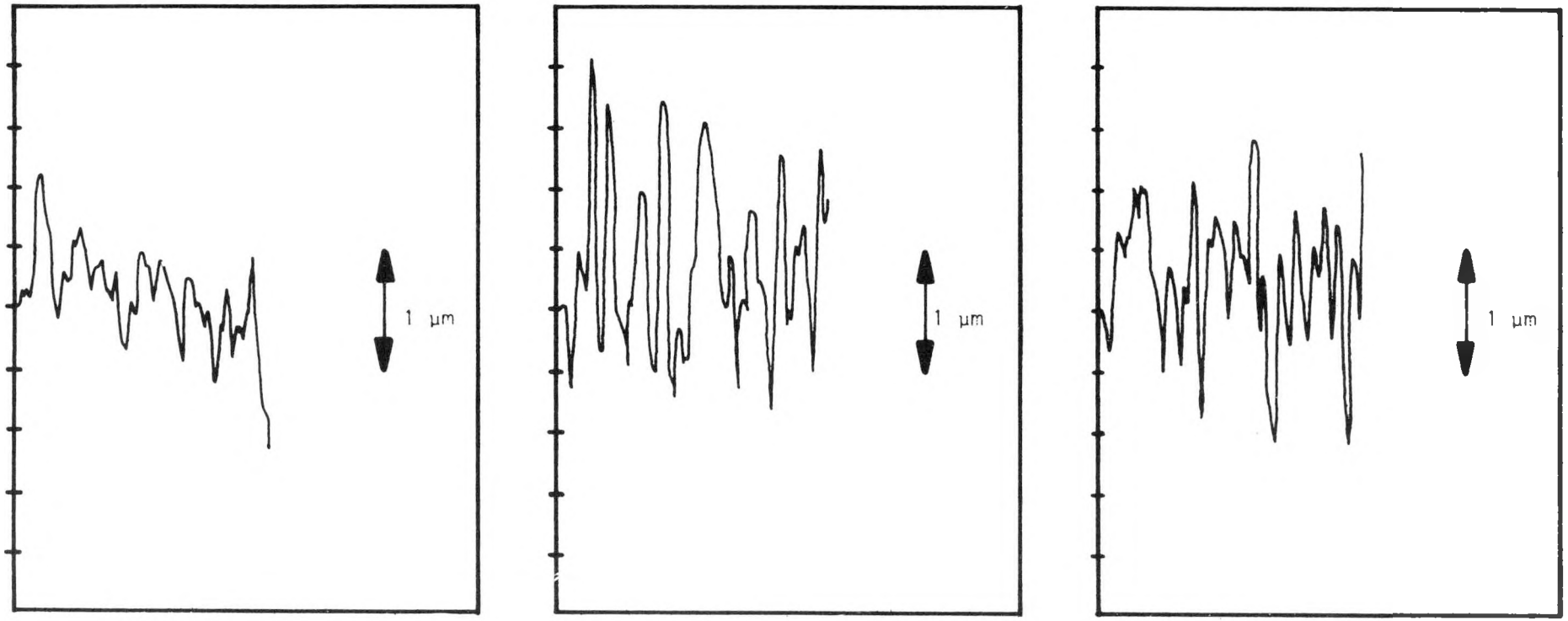

(a) 0.040" Mo as received

(b) 0.040" Mo, etched

(c) 0.040" Mo, etched, Si_3N_4 coated

FIGURE 6: DEKTAK TRACINGS OF 0.040" THICK Mo SUBSTRATES. ALL TRACINGS WERE MADE WITH THE FOLLOWING SETTINGS: Dektak - 2.0 cm/min. Recorder - 10.0 cm/min A^{O} scale - 5 µm full scale.

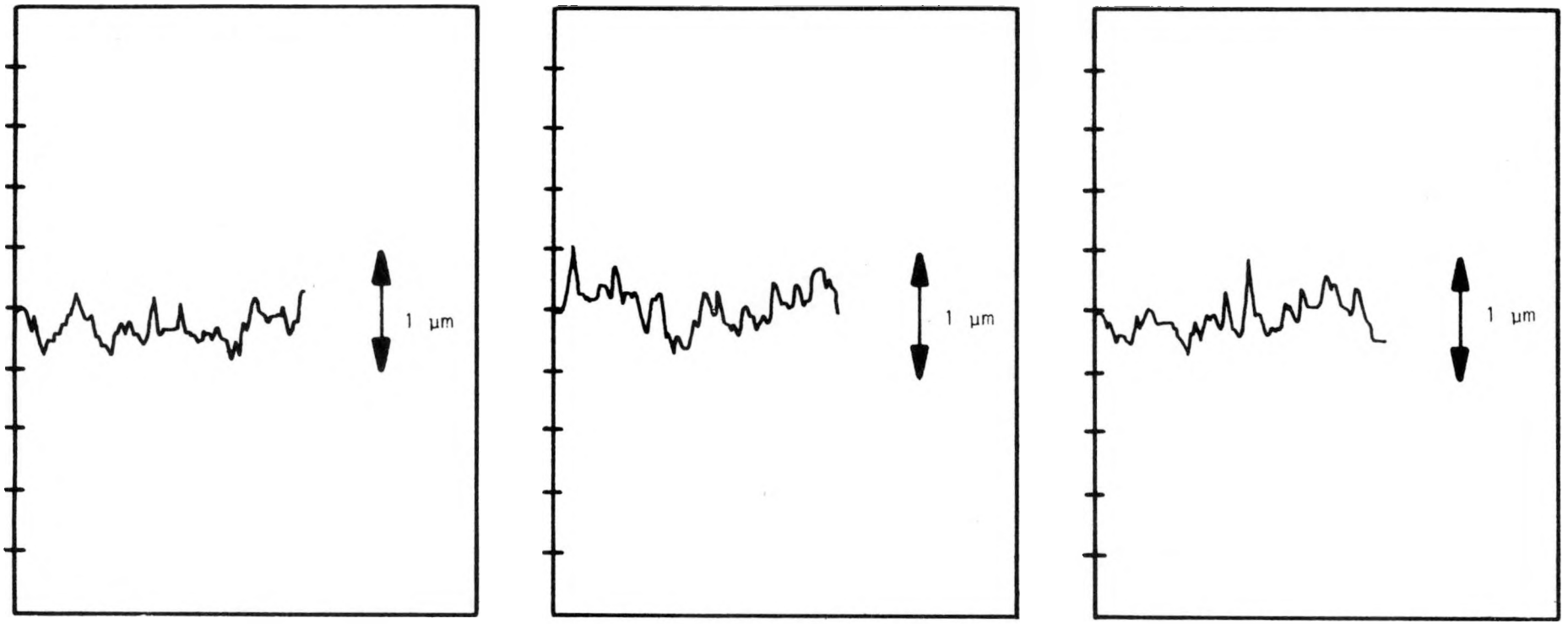

.015" Mo as received

.015" Mo, etched

.015" Mo, etched, Si_3N_4 coated

FIGURE 7: DEKTAK TRACINGS OF 0.015" THICK Mo SUBSTRATES. ALL TRACINGS WERE MADE WITH THE FOLLOWING SETTINGS:
Dektak - 1.0 cm/min Recorder - 10.0 cm/min A^{O} Scale - 5 µm full scale

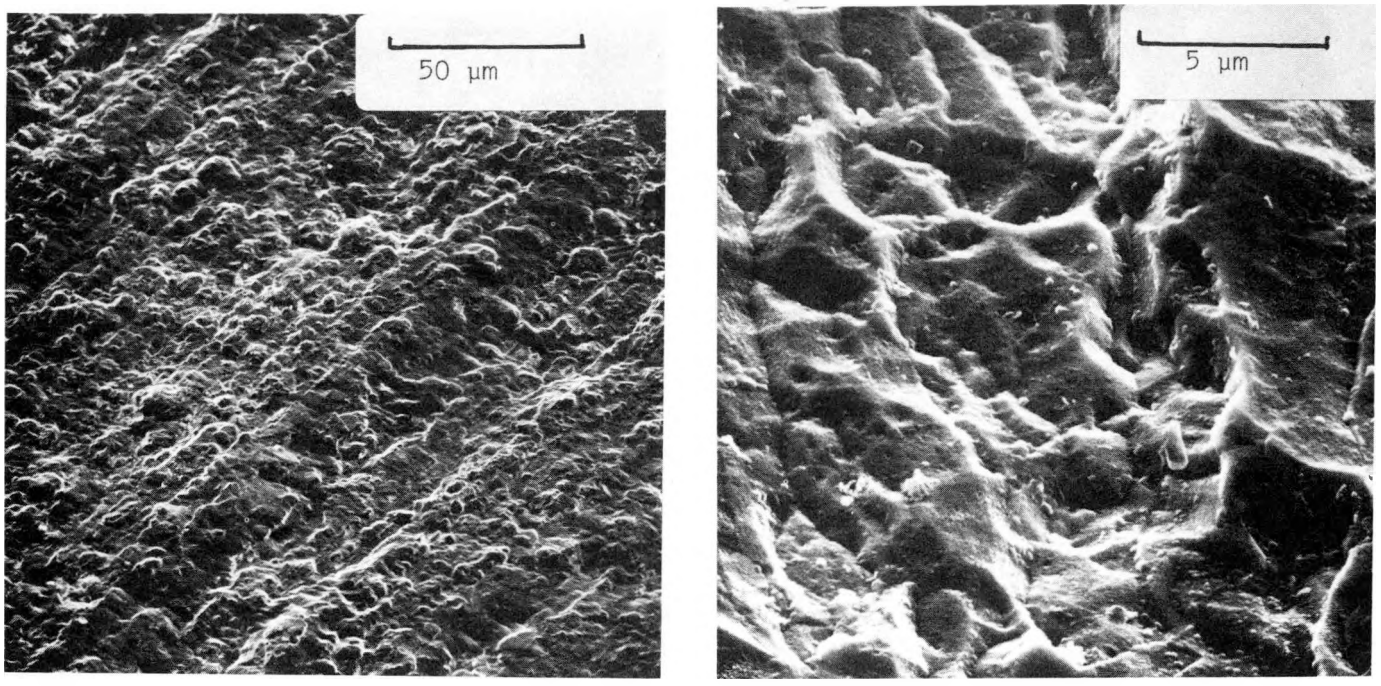

FIGURE 8: SEM PHOTOGRAPH OF AN AS-RECEIVED 0.04" Mo SUBSTRATE. VIEWING ANGLE WAS 45°.

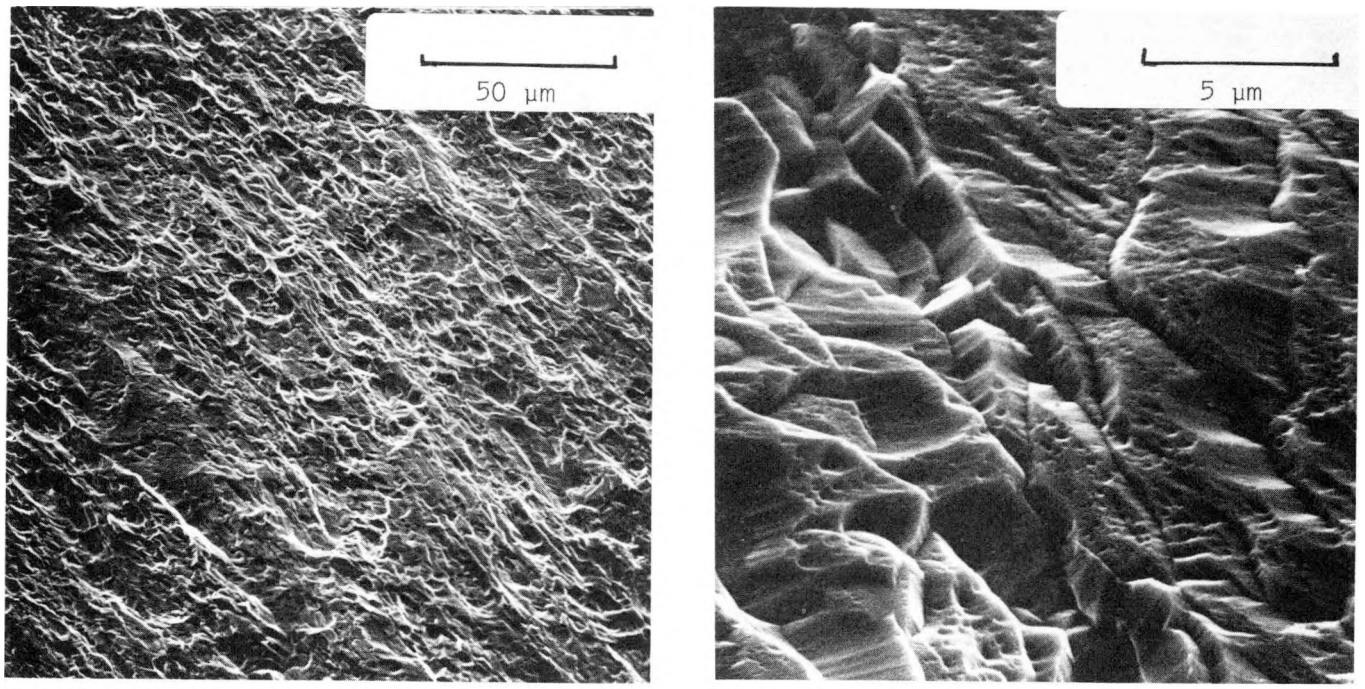

FIGURE 9: SEM PHOTOGRAPHS OF A SOLUTION B ETCHED, 0.04" Mo SUBSTRATE. VIEWING ANGLE WAS 45°.

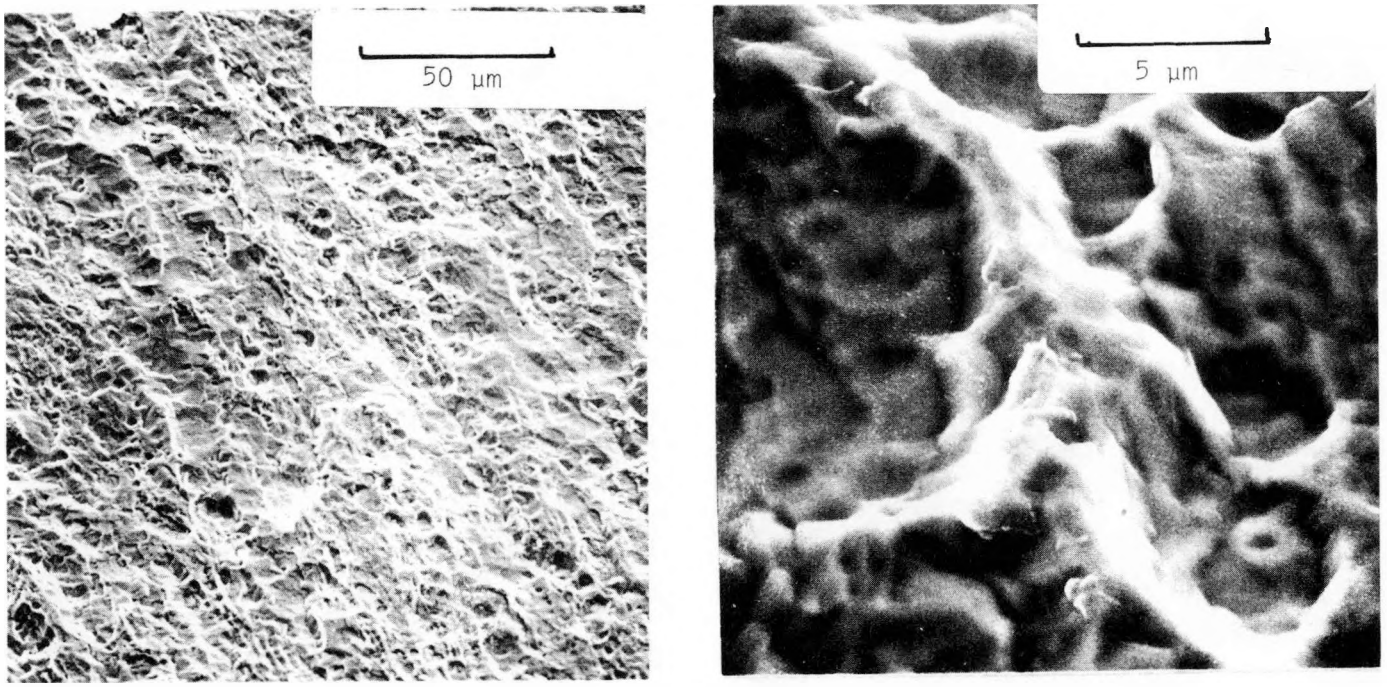

FIGURE 10: SEM PHOTOGRAPHS OF AN ETCHED 0.04" Mo SUBSTRATE AFTER Si_3N_4 COATING. VIEWING ANGLE WAS 45°.

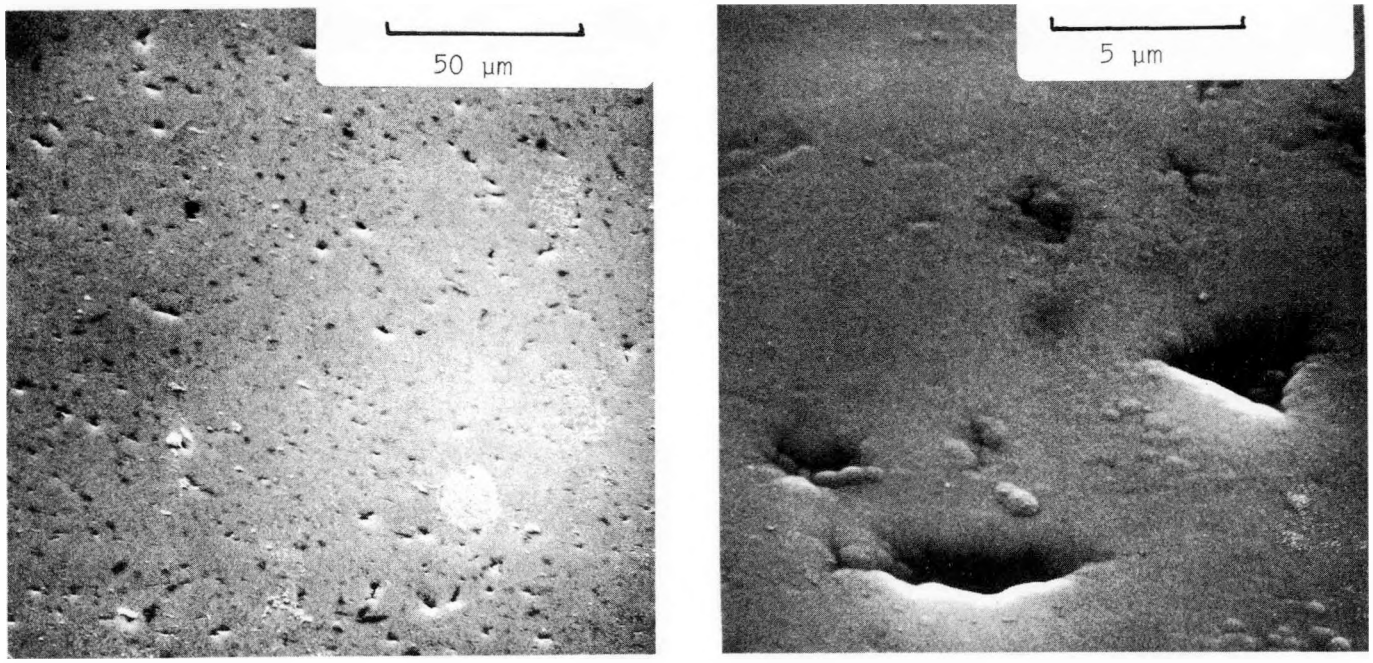

FIGURE 11: SEM PHOTOGRAPHS OF A POLISHED 0.04" Mo SUBSTRATE AFTER Si_3N_4 COATING. VIEWING ANGLE WAS 45°.

Similarly, the $MoSi_2$ separation interface on the polished Mo substrate was found to be smoother after the first deposition cycle than the one on the as-received or etched substrates. However, after a number of deposition cycles, the $MoSi_2$ separation layers on initially polished Mo substrates tended to get rougher similar to the situation with as-received substrates. Thus, initial polishing of Mo substrates was not found to have any significant effect on the recyclability of Mo substrates. Presently it appears that periodic surface smoothing (polishing) of the substrates may be necessary to improve their recyclability. The fact that substrate surface roughness is indeed to be blamed for decreased reliability of separation was proved by unreliable separation observed when using etched substrates.

2.2 DIFFUSION BARRIERS

To prevent continued growth of a $MoSi_2$ layer on the Mo substrate, and also to minimize possible contamination from metallurgical grade Mo substrates, various diffusion barriers were examined for their effectiveness.

2.2.1 SiO_2 BARRIERS

A 0.5 - 1.0 μm layer of SiO_2 was deposited on Mo substrates at 1050°C in a CVD furnace using $SiCl_4$ and O_2 in a H_2 carrier gas; this was followed by silicon deposition at 1150°C. Nucleation was poor, resulting in ribbons with many holes. An SiO_2 layer followed by a thin layer of Si_3N_4 to promote nucleation during deposition resulted in dense, uniform silicon layers which were strongly adherent to the substrate. In fact, the substrate-silicon couple bowed severely from the thermal expansion mismatch. A metallographic section of this substrate (Figure 12) shows the complete absence of silicide formation and the effectiveness of SiO_2 as a barrier.

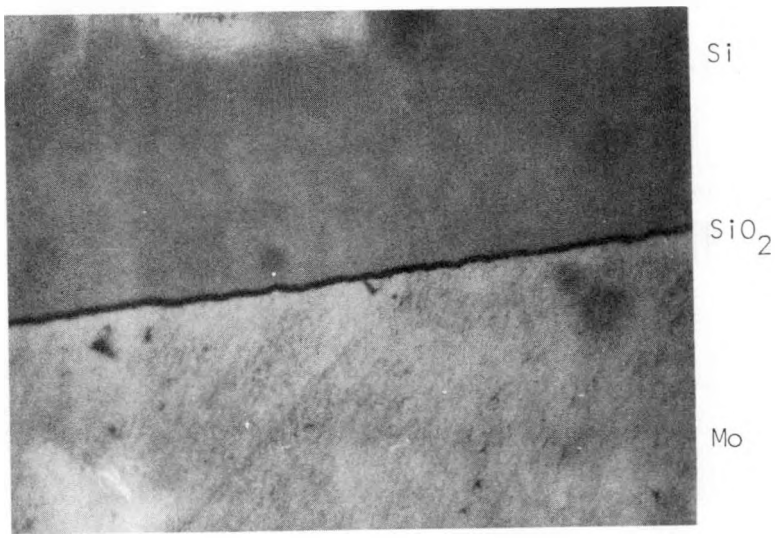

Figure 12: Metallographic Section of an SiO_2 Coated Substrate with Adherent Silicon Film (400X Magnification)

When a few microns thick layer of Si was deposited on Mo, followed by 1 μm of SiO_2 and 10 mils of Si (all carried out successively at 1150° in a CVD furnace), the expected shear separation did not occur. Figure 13 shows a cross-section of this substrate with the adherent silicon film and Figure 14 shows a high magnification SEM photograph of the area circled in Figure 13. It can be seen that almost all of the first silicon layer was converted to $MoSi_2$.

However, when the first silicon layer was made sufficiently thick, ~25 to 50 μm, shear separation took place. A cross-sectional view of this separated silicon film is shown in Figure 15. Only a portion of the intermediate silicon layer, in this case, was converted to $MoSi_2$ and shear separation occurred at the $MoSi_2$-Si interface. The SiO_2 layer between the two layers of silicon can be clearly seen. Samples were etched back through the barrier layer and submitted for neutron activation analysis (General Activation Analysis, Inc., San Diego, California). No Mo was detected in these silicon layers.

2.2.2 Si_3N_4 BARRIERS

Mo substrates were coated with Si_3N_4 by two different methods. The first method utilized SiH_2Cl_2 and NH_3 at 750°C in a low pressure CVD system. The second method used SiH_4 and NH_3 in an Ar carrier at 350°C in a glow discharge. Although the two processes produced nitrides with different etch rates, they both gave comparable results. The Si_3N_4 layer did not form an inpervious barrier since silicide formation occurred. However, it proved beneficial in promoting nucleation for silicon deposition, producing smooth dense ribbons. It also resulted in more reliable shear separation at lower temperatures than for uncoated Mo substrates, particularly on large area ribbons.

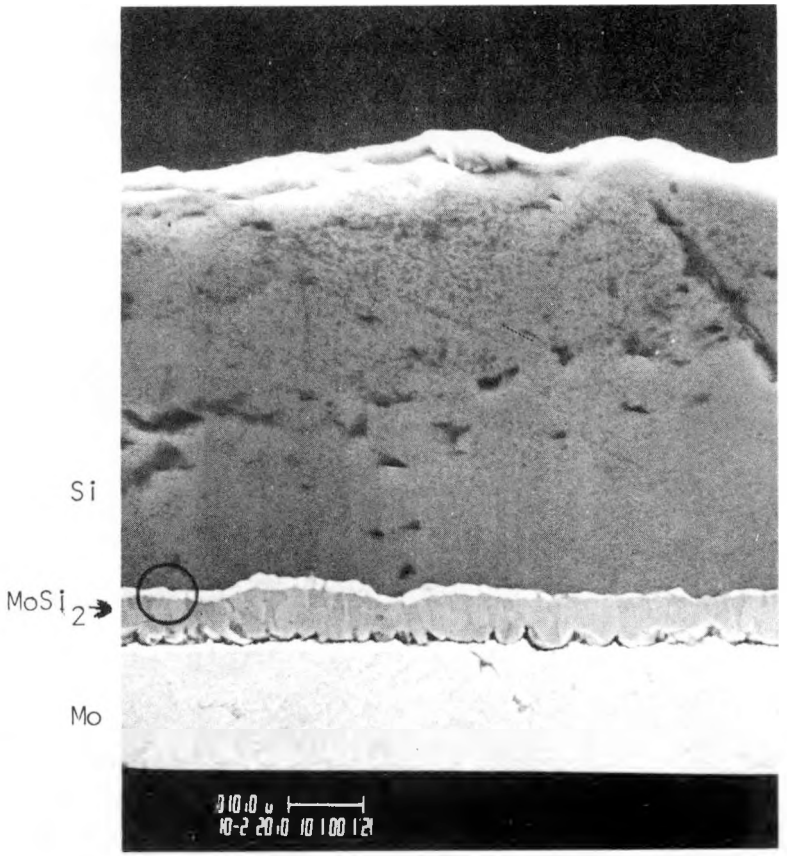

Figure 13: Cross-Section of an Mo Substrate Using SiO_2 Diffusion Barrier with Adherent Silicon Film

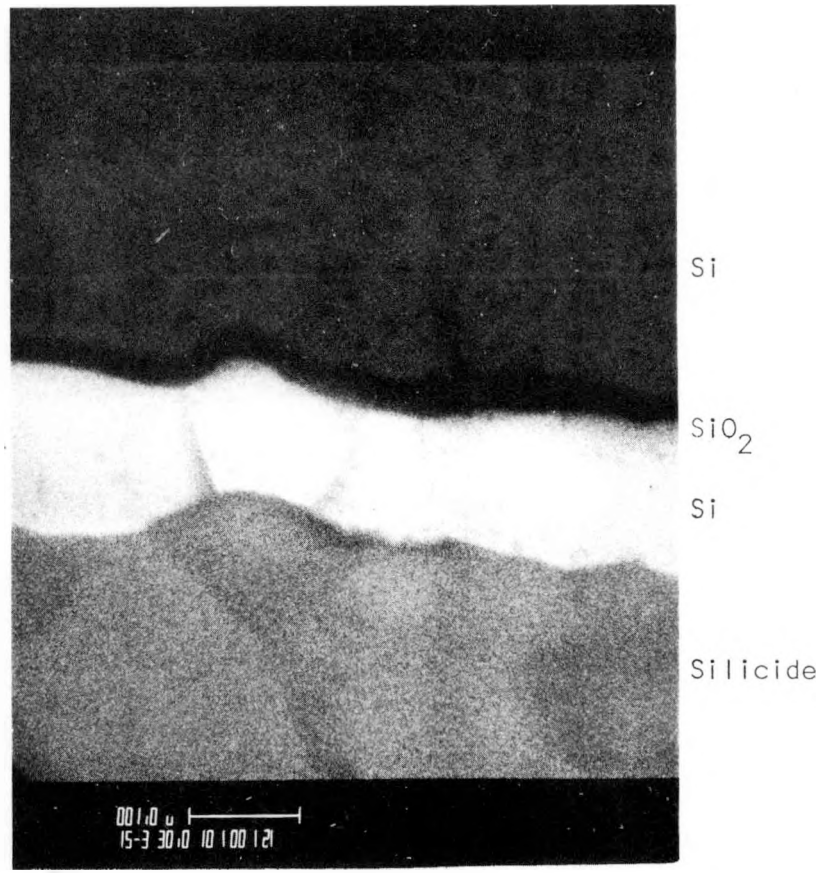

Figure 14: High Magnification (15000X) SEM Photograph of the Area Circled in Figure 6

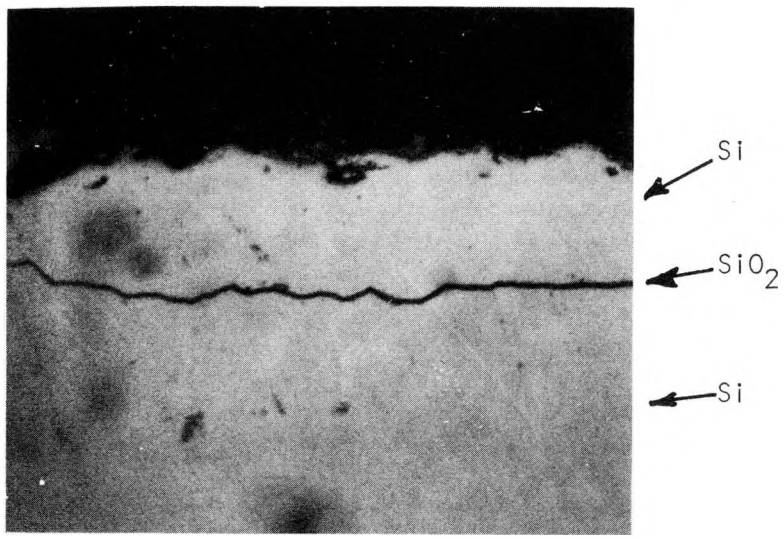

Figure 15: Cross-Section of a Silicon Film Separated from an Oxide-Coated Substrate (400X)

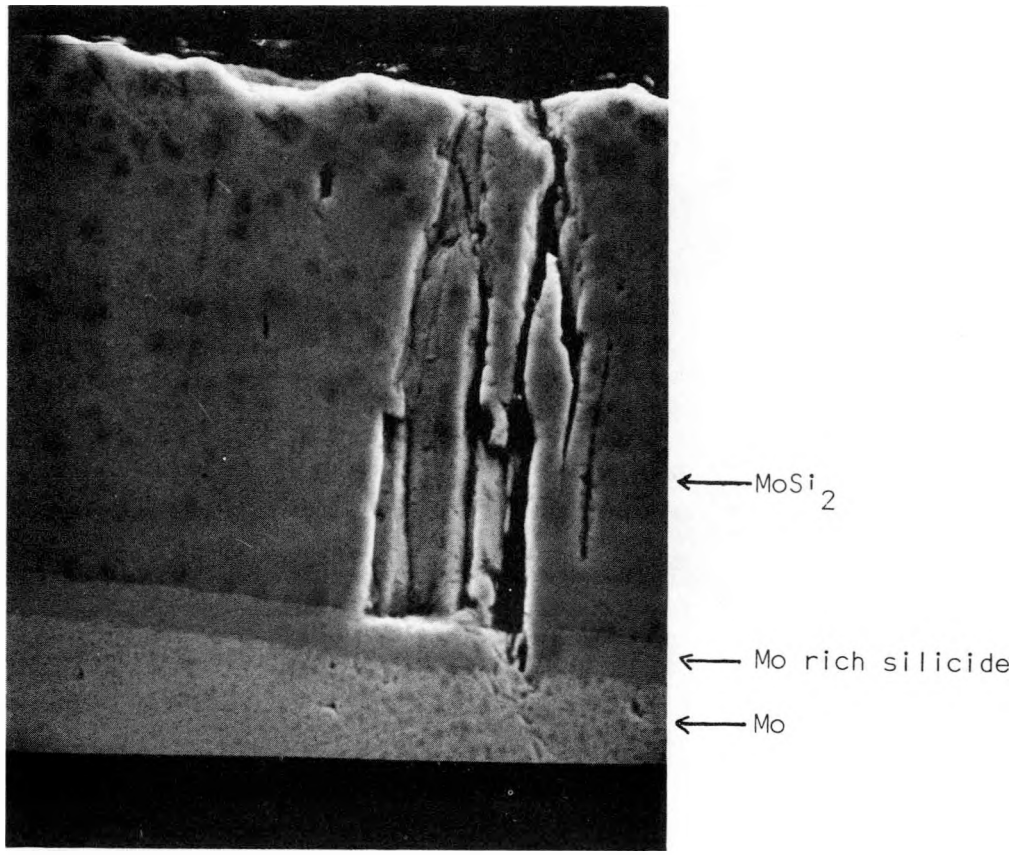

FIGURE 16

Cross-section of an Al_2O_3 coated Mo substrate after one silicon deposition cycle.

2.2.3 Al_2O_3 BARRIERS

Al_2O_3 has been used successfully as a diffusion barrier in germanium processing (10), and since it is a refractory material it seemed potentially promising as a barrier layer. Mo substrates with 2500Å and 5000Å layers of Al_2O_3 were prepared by reactive sputtering. In both cases deposited Si ribbons sheared off. SEM photographs of the substrate cross sections were similar to those of uncoated Mo substrates with apparent silicide formation (Figure 16). X-ray diffraction patterns from the substrate surface clearly identified the layer as $MoSi_2$ and thus Al_2O_3 was ineffective as a diffusion barrier at 1150° deposition temperatures.

2.3 COMPOSITE TESS SUBSTRATES

By employing a composite substrate with various layers chosen for specific functions, the mechanical and shear separation properties of the substrate can be independently controlled. Figure 17 shows one of the possible configurations of this substrate. The characteristic features of this configuration are:

1) It employs a Mo substrate core which can be thin enough to be flexible for use as a belt type substrate, or thick enough to be rigid.
2) A thin SiO_2 layer acts as a diffusion barrier preventing diffusion of impurities from the Mo substrate into the Si, and prevents any reaction between the substrate (core) and the silicon deposit. Because the Si-O bond is stronger than Mo-O bond, the integrity of SiO_2 on Mo is assured.

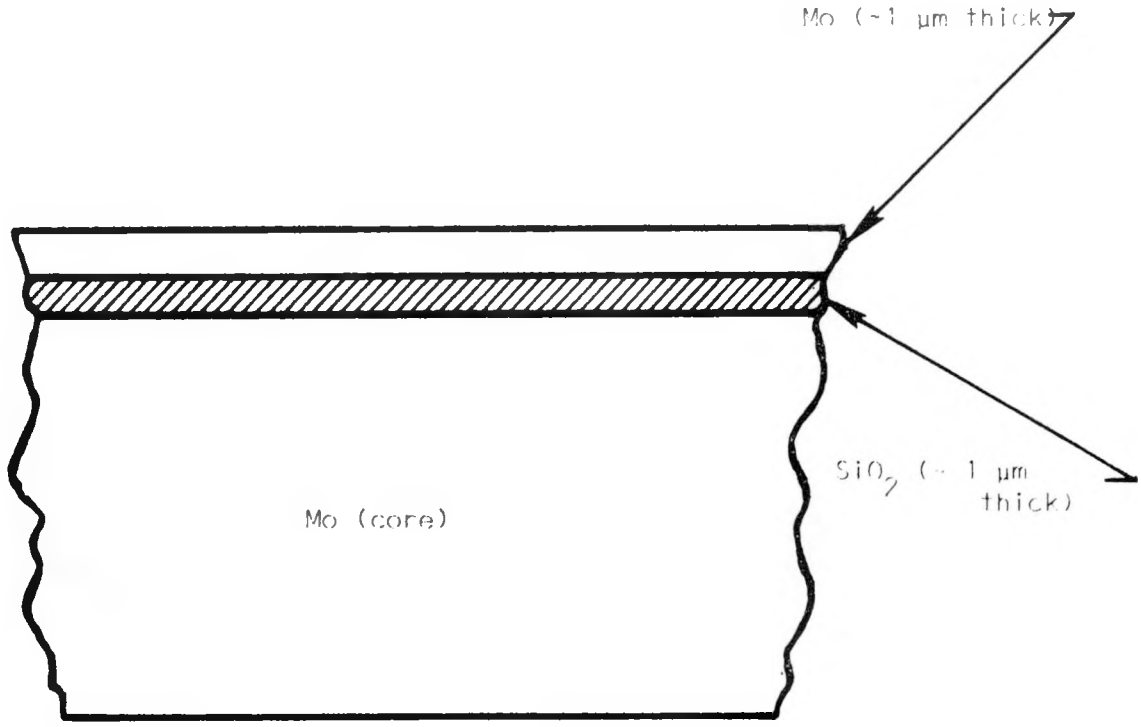

FIGURE 17: Schematic cross-section of a composite substrate utilizing SiO_2 diffusion barrier.

3) A thin, high purity Mo layer is deposited on top of the SiO_2 diffusion barrier. During silicon deposition, this will be converted into $MoSi_2$ and acts as a shear separation interface.

Composite substrates Mo (40 mils): SiO_2 (~ 1 μm): Mo (3000Å) have been fabricated, and shear separation has been successfully demonstrated. The thin SiO_2 layer was deposited by chemical vapor deposition from $SiCl_4$ and O_2 at 1150°C. The thin Mo film was deposited by sputtering.

As these composite substrates were subjected to successive silicon deposition cycles, the $MoSi_2$ layer peeled off at a few small spots, exposing the (colored) oxide. Then, during a subsequent silicon deposition cycle, the silicon deposit adhered at the spots where the oxide was exposed. Thus, for complete recyclability of this composite substrate, the $MoSi_2$ separation layer must be continuous and adherent to the oxide. Hence, optimizing the composite substrate parameters for $MoSi_2$-SiO_2 adherence is important.

A sample of a silicon ribbon separated from one of these composite substrates, with 10 μm etched from the surface, was submitted for Neutron Activation Analysis. It contained 0.39 ppm of Mo, which is comparable to the results obtained from ribbons separated from conventional Mo substrates and etched the same amount.

Auger analysis was also used to characterize the composite substrates for individual layer compositions and their thicknesses. Figures 18 and 19 show examples of the results. Figure 18 shows the composition profile from a composite substrate which was supposed to be a thin SiO_2 on top of the Mo substrate. Presence of a molybdenum oxide layer in place of the SiO_2 layer can be clearly seen in the Figure. Thus in this case instead of depositing SiO_2, a molybdenum oxide was formed due to lack of control in SiO_2 deposition conditions. Figure 19 shows the composition profiles from a composite

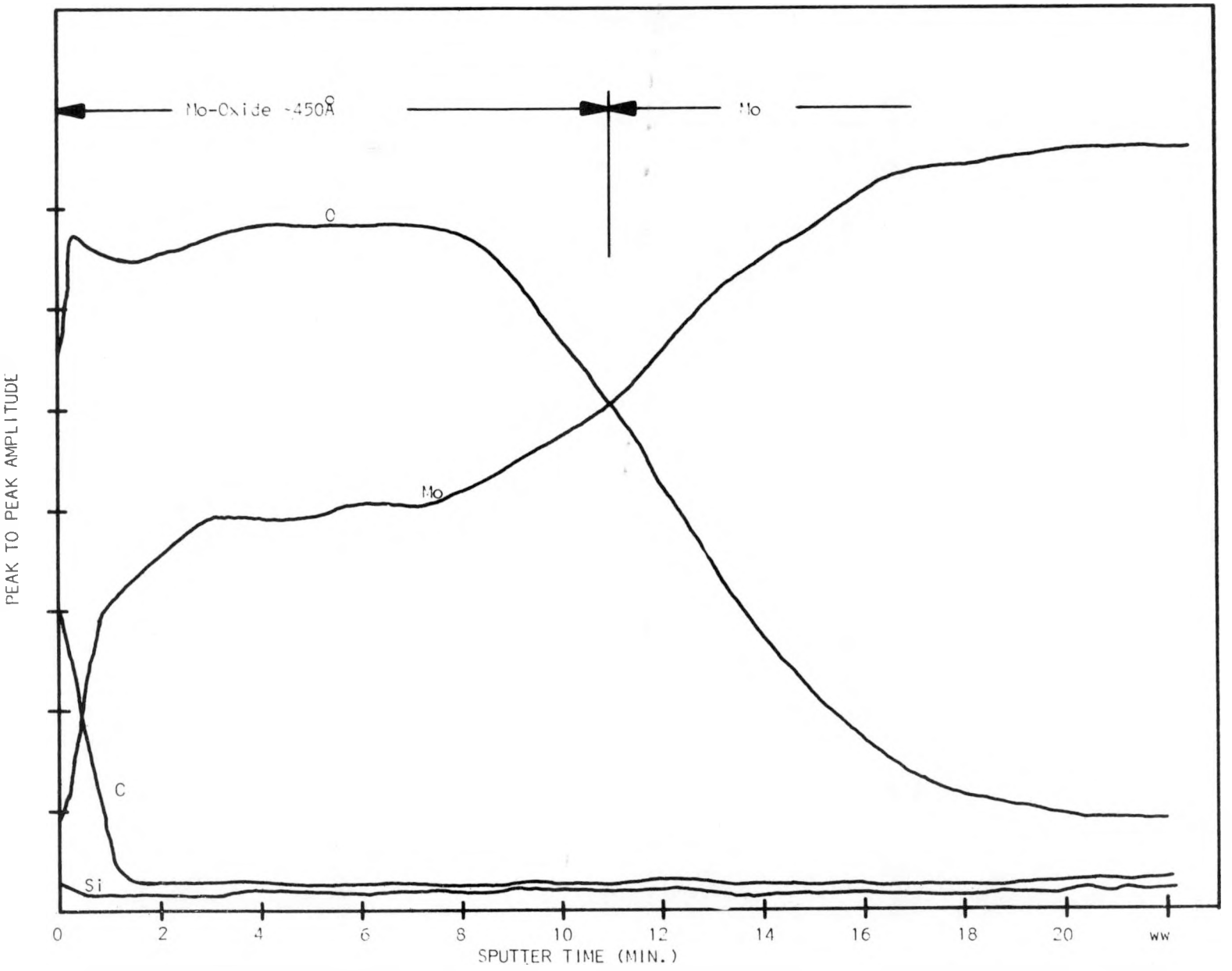

FIGURE 18: AUGER CONCENTRATION PROFILE FROM A CMPOSITE SUBSTRATE WHICH WAS SUPPOSED TO BE Mo (THICK)/ SiO_2 (THIN). PRESENCE OF Mo-OXIDE IN PLACE OF SiO_2 CAN BE CLEARLY SEEN IN THIS FIGURE.

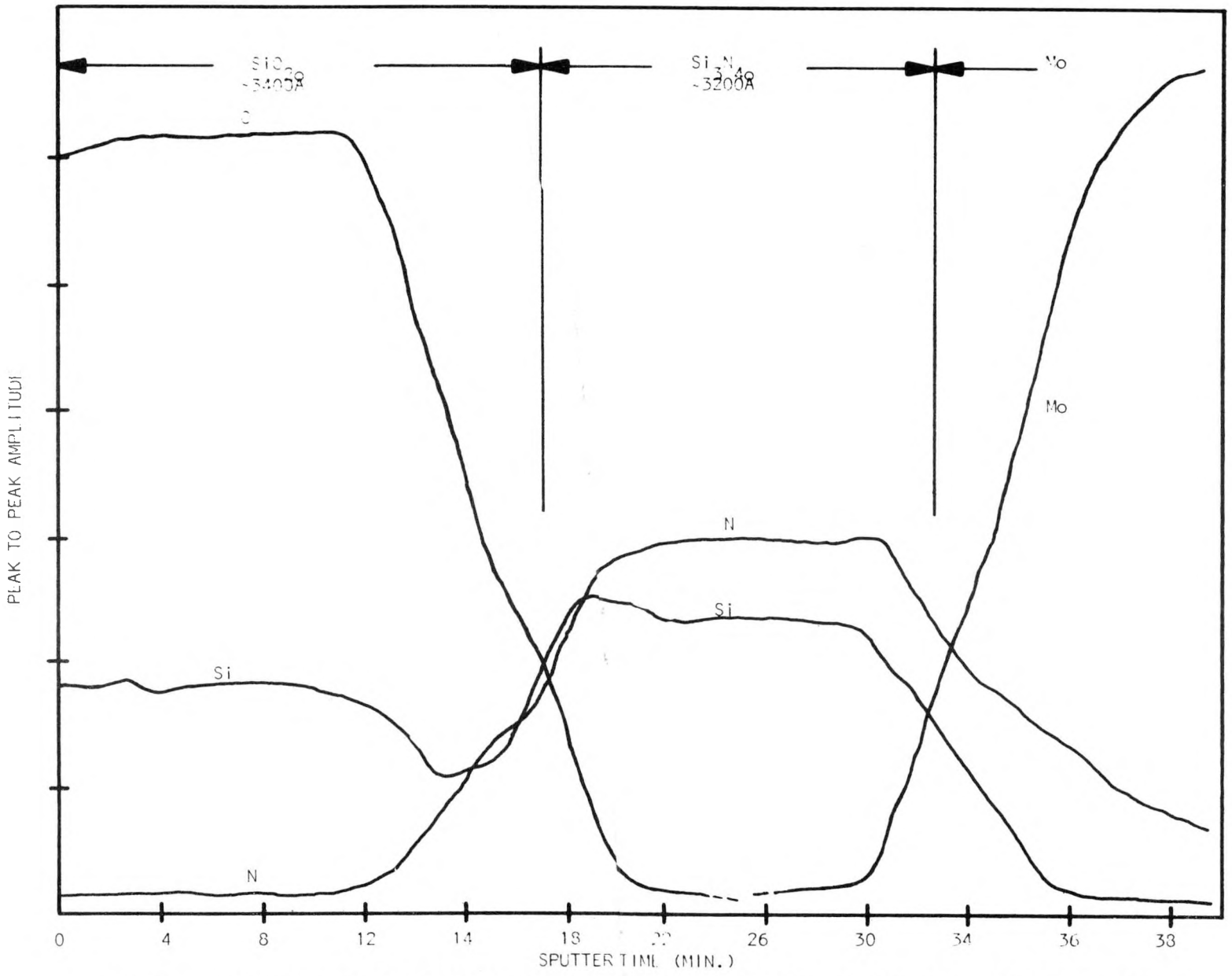

FIGURE 19: AUGER CONCENTRATION PROFILE FROM A COMPOSITE SUBSTRATE Mo (THICK):Si_3N_4 (THIN):SiO_2 (THIN)

substrate - Mo (thick): Si_3N_4 (thin): SiO_2 (thin). The presence of individual thin layers can be clearly seen and their thickness estimated from this profile. Thus Auger analysis has proven to be useful for characterizing the composite substrates and correlating these results with observations on shear separation characteristics.

2.4 NOVEL SUBSTRATES

2.4.1 PLASMA SPRAYED Mo ON STAINLESS STEEL

A silicon deposition experiment using a molybdenum-coated stainless steel substrate was carried out in the Energy Beam System at 1100°C. The substrate was prepared by plasma spraying 3 mils of Mo on type 304 stainless steel. Problems were encountered in the system due to an O-ring failure and air leakage into the system. Even though the film and substrate were grossly contaminated, it appeared that the film separated from the substrate. Upon repeating the experiment in a conventional CVD system at 1100°C, the Mo coating was found to be porous to silicon as indicated by a reaction between silicon and stainless steel.

2.4.2 SPUTTERED Mo ON Al_2O_3 SUBSTRATES

Alumina substrates with 10,000Å of sputtered Mo were used for Si deposition at 1150°C. The silicon sheared from the substrate clearly with no metal remaining on the substrate. It appears that the shearing takes place because of a weak bond between the Al_2O_3 and $MoSi_2$. X-ray diffraction of the ribbon surface next to the substrate indicated the presence of $MoSi_2$, Mo_5Si_3 and Si.

2.4.3 CVD Mo ON GRAPHITE

Substrates were prepared by depositing CVD Mo on HPD-1 Poco graphite. The Mo deposition was carried out by H_2 reduction of $MoCl_5$ at 825°C. Figure 20 illustrates the system used. $MoCl_5$ was vaporized and carried through heated tubing by argon to the furnace where it was mixed with H_2. Shiny adherent films were deposited on the quartz reaction chamber and a matte surface was obtained on the graphite. Silicon deposition, at 1150°C, on this substrate resulted in a cleanly sheared ribbon. X-ray diffraction of the sheared silicon surface revealed only silicon lines in the diffraction pattern. The sheared surface of the substrate showed a diffraction pattern for $MoSi_2$. The shear mechanism in this case needs further investigation.

2.4.4 POWDERY SILICON COATINGS

In the energy beam system, a fine powdery silicon is deposited in the cool exit end of the reaction tube. This has been collected and a slurry made from it with water. Mo substrates painted with the slurry produced good sheared ribbons. In order to test whether it was indeed a good release agent, on Al_2O_3 and a fused silica substrate were coated with a slurry, dried, and put through a deposition cycle. In both cases the deposited Si stuck to the substrates and shattered in cooling. Microscopic examination of the Si, through the clear quartz, showed no trace of the original brown colored silicon layer. It had apparently been densified during the deposition. With the Mo substrates therefore, a normal silicide layer was formed and standard shear separation took place.

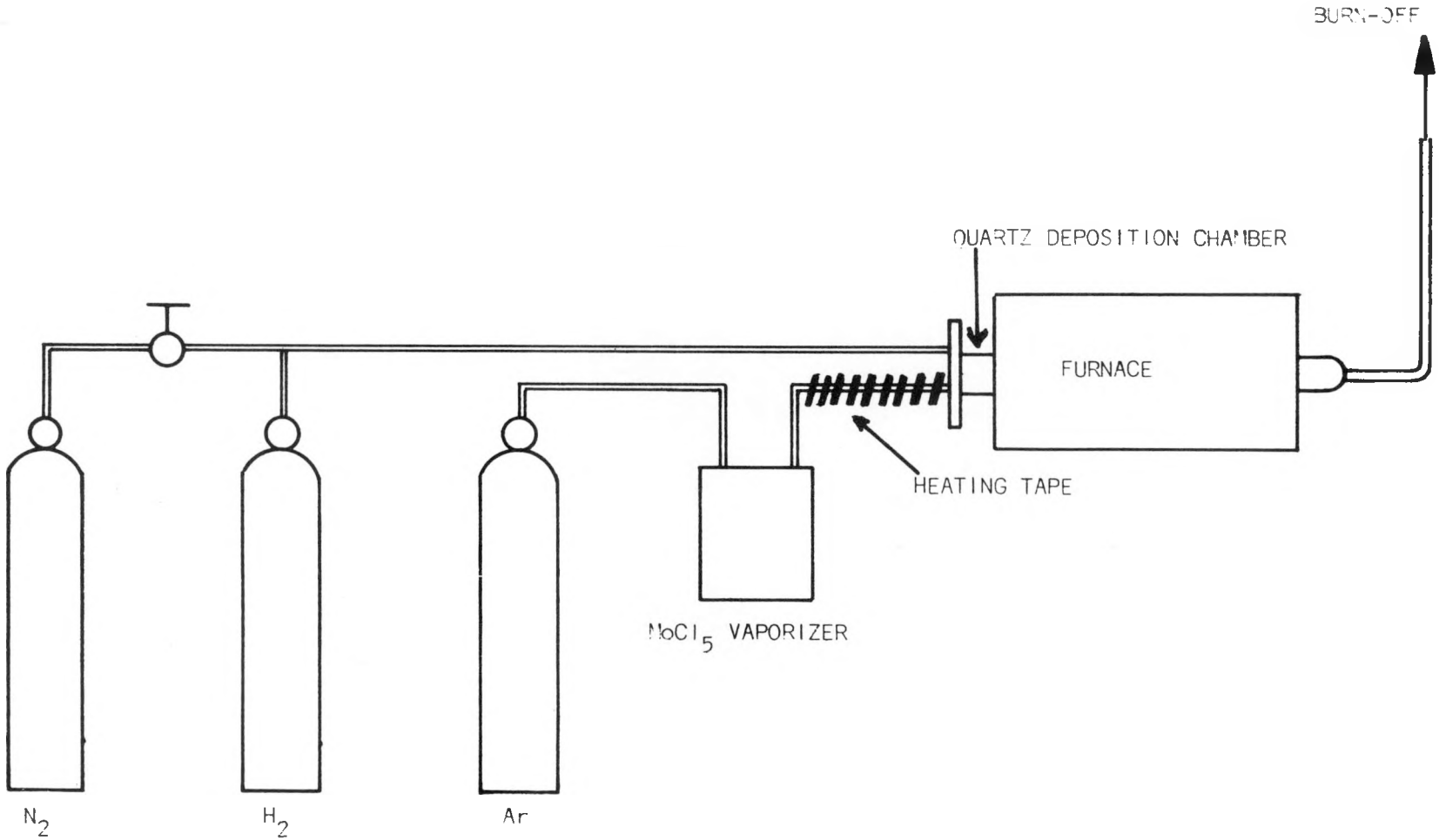

FIGURE 20: SCHEMATIC OF A CVD SYSTEM FOR DEPOSITING THIN HIGH PURITY Mo FILMS.

2.5 CONTINUED RELIABILITY OF SHEAR SEPARATION

For economic reasons, Mo substrates must be capable of being used many times. Multiple depositions have been made on hundreds of substrates but, with continued use, shear separation becomes less reliable. The usual "failure mode" for a substrate is that, after several whole ribbons have been produced, a cracked ribbon results. That is, all of the silicon shears from the substrate but the ribbon shears off in two or more pieces. A further deposition on the same substrate then results in sections of the silicon ribbon strongly adhering to the substrate and the remainder of the ribbon shattering. Figure 21 shows an SEM photograph of a silicon ribbon which cracked, and the substrate from which it sheared. Silicon "islands" adhering to the $MoSi_2$ layer, and craters in the silicon ribbon, are clearly visible and are the onset of the failure mode. Figure 22 shows the relative increase in thickness of $MoSi_2$ with multiple runs. One possibility for the failure mechanism is that silicon diffusion becomes less and less with the increasing $MoSi_2$ layer thickness, with a smaller size and/or concentration of voids being formed in the silicon. Since the interface will be stronger with fewer voids, the interfacial thermal stresses due to expansion mismatch are not sufficient to cause fracture at the $MoSi_2$-Si interface, thus resulting in silicon ribbon adherance to the substrate.

The $MoSi_2$ layer was removed from several failed substrates by surface grinding. Succeeding depositions were carried out with normal shear separation taking place. Thus Mo substrates can be refurbished for continued use by removal of the $MoSi_2$ layer. Since SiO_2 layers had been shown to cause adherence of the ribbon, there was a possibility that the $MoSi_2$ may have formed a thin layer of SiO_2 if the substrates were removed from the CVD furnace at too high a temperature. Four substrates were selected that had failed by ribbon cracking. They were etched in HF for five minutes and then used for silicon deposition. Three of the four

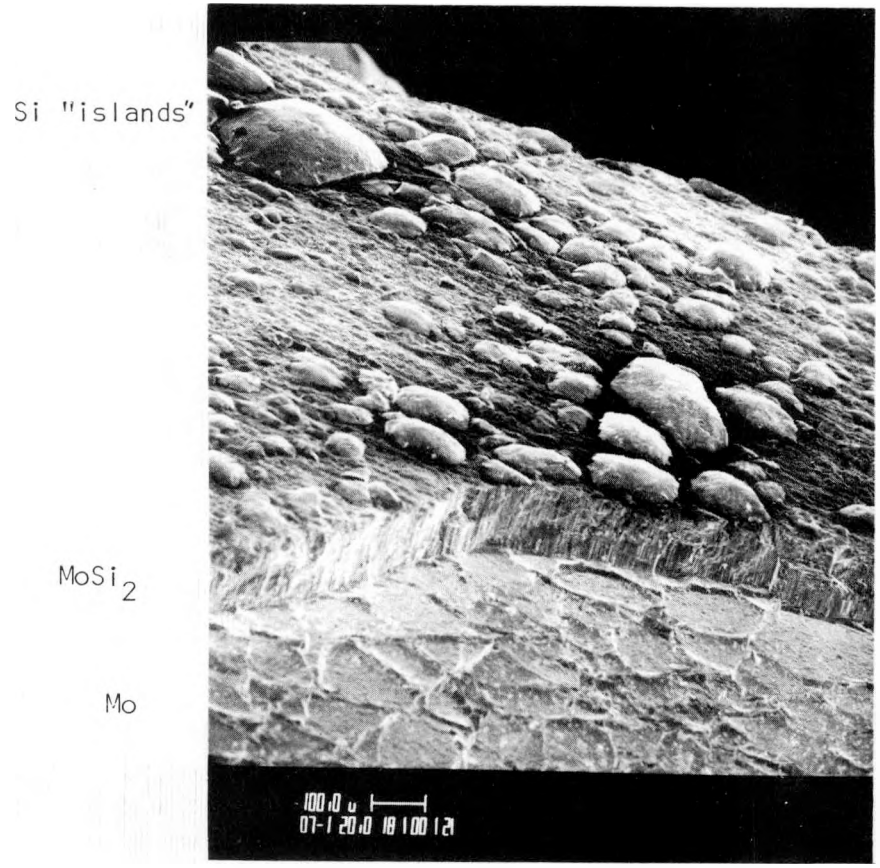

Mo substrate surface
70X

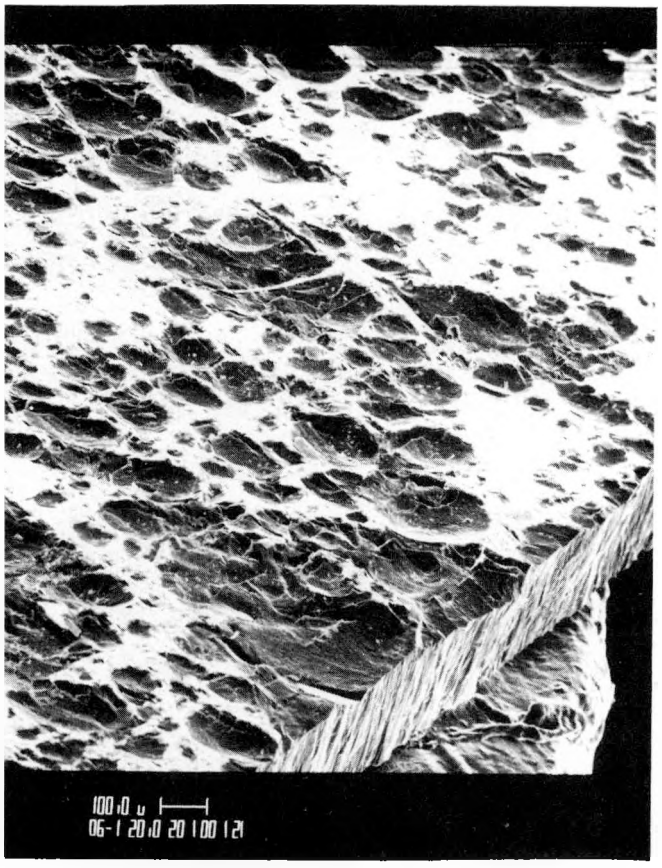

Sheared surface of silicon ribbon
60X

FIGURE 21

SEM Photographs of Cracked Silicon Ribbon and the Substrate that Produced it.

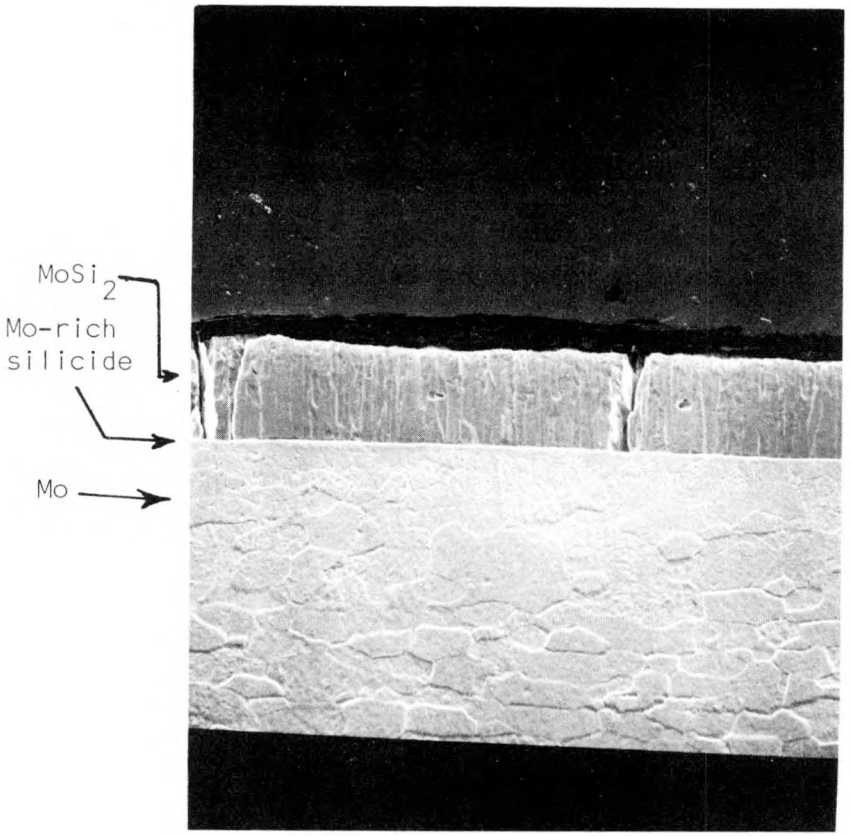

SUBSTRATE CROSS-SECTION
USED 1 TIME 320X

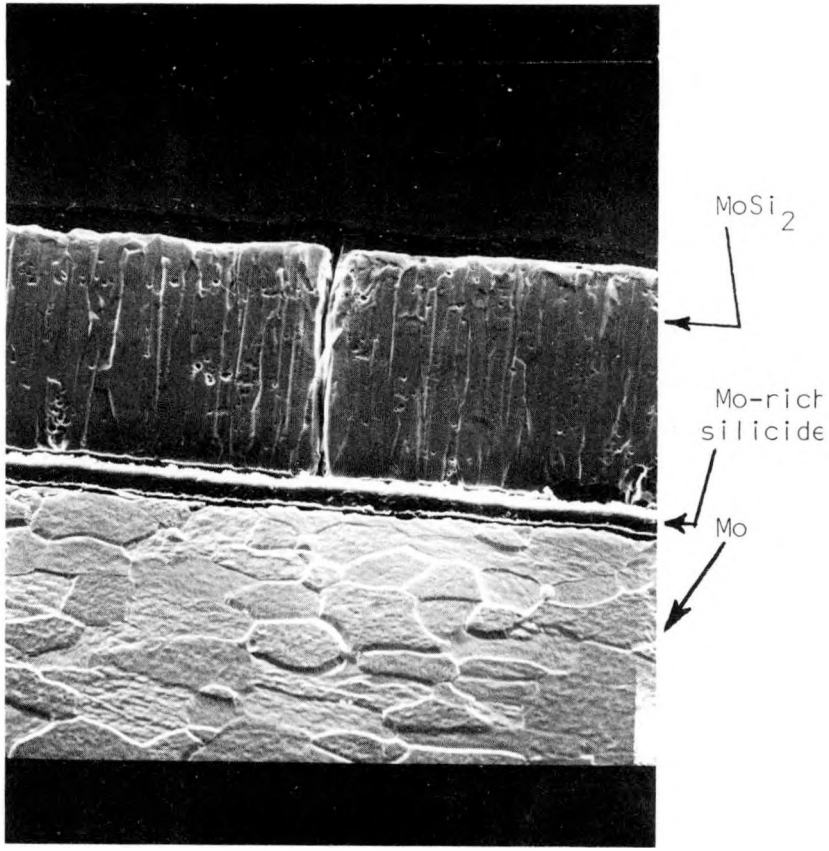

SUBSTRATE CROSS-SECTION
USED 4 TIMES 320X

FIGURE 22

Increase in Thickness of $MoSi_2$ Layer with Repeated Use of the Substrate.

produced good ribbons where it would normally be expected to have ribbon adherence and/or severe breakage. After HF etching a second time, a deposition produced all cracked ribbons.

Two substrates were selected after one deposition. One was oxidized in air at 1000°C for 1 minute. (The substrate was pushed into an open tube furnace and left for 1 minute, so it is doubtful that the substrate temperature reached 1000°C.) The two substrates were used in the same deposition and the silicon stuck severely to the oxidized substrate. Further investigation needs to be made on the role of the $MoSi_2$ surface prior to deposition.

Composite substrates and novel substrates, in which the surface is prepared prior to each deposition, would have reliable shear separation. If the cost of surface preparation is small, composite substrates would then be a satisfactory alternative to Mo substrates.

3.0 ENERGY BEAM DEPOSITION

The Energy Beam Deposition process for microcrystalline silicon film deposition has been described in detail previously (9). During this year, a batch type EBD system has been investigated, both in horizontal and vertical modes of operation. Near the end of the year a continual EBD system was designed, fabricated and tested. Methods of making reliable temperature measurements (in the RF plasma ambient) during deposition have been developed. The multiple electrode nozzle and the rotating nozzle have been further examined for their effectiveness in minimizing beam arcing problems. EBD parametric studies have been conducted using $SiHCl_3$ as the silicon bearing gas. All the silicon films were doped with B_2H_6 during deposition. The as-deposited and shear-separated silicon ribbons were characterized for their morphology and microstructure.

3.1 BATCH EBD SYSTEMS

The basic geometry (i.e. Energy Beam plasma flowing parallel to the substrate surfaces) of the horizontal and vertical energy beam systems is still the same as described in reference (9). However, the short (12" long) single zone furnaces in the previous systems were replaced with longer (24" long) three-zone furnaces. The new furnaces have a 3" diameter aperture. Reactor tubes of various sizes and cross-sections can be placed in this furnace by using appropriate ceramic vestibule blocks. The three control thermocouples are located at approximately 3", 12" and 18" from the beginning of the (24" long) heating element. All the deposition experiments were conducted using a square-cross section quartz deposition chamber with an expanded portion (9) near the nozzle. The deposition chamber is approximately 4 cm x 4 cm in cross-section. The walls of this chamber are covered with four 0.1 cm thick molybdenum substrates, which are in turn held in position by small molybdenum clips placed at the corners. This same substrate arrangement is used both in the horizontal and vertical EBD systems.

3.2 SUBSTRATE TEMPERATURE

Substrate temperature is an important parameter of the deposition process because of its effects on deposit morphology and the shear separation process. For a successful deposition process, a zone of uniform temperature is required. In the EBD system, the resistance furnace as well as the Energy Beam plasma contribute to substrate heating. The amount of beam contribution depends on its RF power and the reactant gas flow rate. Since the Energy Beam is used primarily for deposition process enhancement, the substrate temperature is controlled by the furnace controllers while maintaining a constant RF beam power and constant reactant gas flow rates. To investigate the effects of plasma beam RF power, furnace controller settings, and reactant gas flow rates, temperature profiles in the deposition chamber were determined in both horizontal and vertical EBD systems. The distance from the energy beem nozzle to the beginning of the heating element was maintained at approximately 6".

Temperature profile in the deposition zone was first measured by moving a chromel-alumel thermocouple contacting the inside wall of the deposition chamber. A.C. voltages induced into the measuring thermocouple by the RF plasma beam interfered with the performance of the temperature-indicating instrument and, as a result, completely meaningless results were obtained. When the induced a.c. voltages were filtered out by an LC filter placed between the thermocouple and the indicating instrument, the measured temperatures were within 10°C of the actual temperature. (The actual temperature was determined by a measurement made immediately after the RF plasma beam was completely turned off.) Shielding the thermocouple by an insulated metal tube resulted in no RF interference, and the measured temperature corresponded exactly to the actual temperature. Hence, all temperature measurements were made with a shielded thermocouple.

Figure 23 shows examples of some of the profiles determined in the horizontal EBD system when all three of the furnace controllers were set at 1100°C. Profile A was obtained with a hydrogen flow rate of 2 LPM* and a beam RF power of zero (i.e., in the absence of a plasma beam). The temperature in most parts of the deposition zone was very uniform (1100° ± 2°C). The temperature in the first 3" of the deposition system was very low because of the cold H_2 entering the system from this side. (When no gas was flowing through the system, the temperature profile was very symmetric, as expected.) In open flow deposition system, the length of the developing temperature region depends on the flow rate of the reactant gas and the aspect ratio (ratio of the length of the deposition system to its cross-sectional size). For a fixed flow rate, the developing temperature region decreases with increase in aspect ratio and vice-versa. Profile B shows the effect of a higher gas flow rate (25 LPM of H_2). In this case the developing temperature region is extended to more than half the length of the deposition system and only a short length of uniform temperature zone is obtained. Profile C was obtained with H_2 flow = 25 LPM and RF = 2.5kW. Note the length of the developing temperature region; the small developing temperature region is due to preheating of the gases by the energy beam plasma. In this case, even though the control thermocouples were indicating a temperature of ~ 1100°C (set point), the deposition zone temperature was raised to 1150°C. This is because of preheated (by the energy beam) hydrogen flowing through the deposition system. However, when the RF power is reduced to 2.0 kW (profile D) to reduce gas preheating, temperatures in the deposition zone corresponded with the furnace controller set point. Similar effects were observed in temperature profiles in the vertical EBD system. After the initiation of silicon deposition (introduction of $SiHCl_3$ and B_2H_6 into the plasma), the substrate temperature was found to gradually increase (by up to 15°C) and stabilize.

*LPM = Liters per Minute

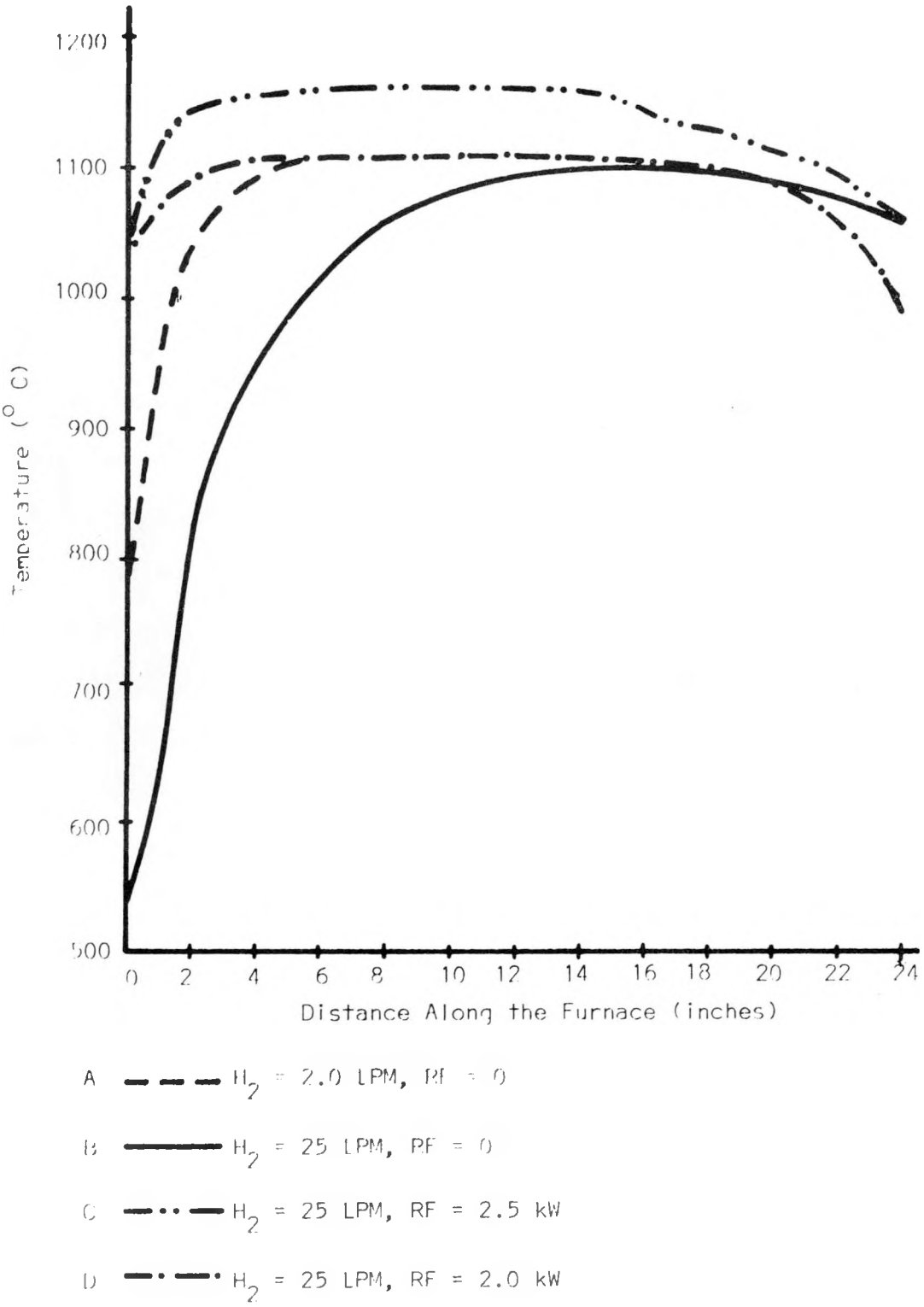

Figure 23: Temperature Profiles in the Horizontal EBD System When All Controllers Were Set at 1100 °C

3.3 DEPOSITION PARAMETRIC STUDIES

The effects of substrate temperature and RF power of the plasma beam were reported in reference (9). During this year the effects of input chlorosilane concentration and total reactant gas flow rate were more thoroughly investigated.

The effect of input $SiHCl_3$ concentration (given as $\frac{Cl}{H}$ ratio) on the efficiency of deposition (calculated from weight gain measurements) is shown in Figure 24. In these experiments, the total gas flow rate, RF power of the plasma and the substrate temperature were maintained constant at 25 LPM, 2.5 kW and 1150°C respectively. The solid curve shows the calculated efficiency when equilibrium in the gas phase is assumed (9); i.e. this curve indicates the maximum possible efficiency obtainable in a conventional CVD process at 1150°C, using $SiHCl_3$. When compared to the equilibrium curve, the average EBD efficiencies were higher by a few percent (0 to 5%) for $\frac{Cl}{H}$ ratios < 0.12, and lower by a few percent for $\frac{Cl}{H}$ ratios > 0.12. In best individual runs, deposition efficiencies are higher by up to 12% compared to the equilibrium efficiency.

Figure 25 shows the effect of total gas flow rate on the deposition efficiency for horizontal and vertical orientations of the EBD system when the input $\frac{Cl}{H}$, RF power of the beam, and the substrate temperature were maintained constant at 0.1, 2.5 kW and 1150°C respectively. For a given flow rate, the efficiency in a vertical configuration was lower than in a horizontal configuration by up to 7%. However, in both cases efficiency decreased with increase in flow rate. Deposition rate in μm was calculated from the thickness of the separated silicon films. Figure 26 shows a typical deposition rate profile along the center line of the substrate. This profile was obtained with a total gas flow rate of 25 LPM, $\frac{Cl}{H}$ ratio of 0.1, B_2H_6 (10 ppm in H_2) flow of 0.24 LPM, RF power of 1.5 kW and a substrate temperature of 1150°C. The deposition rate increases

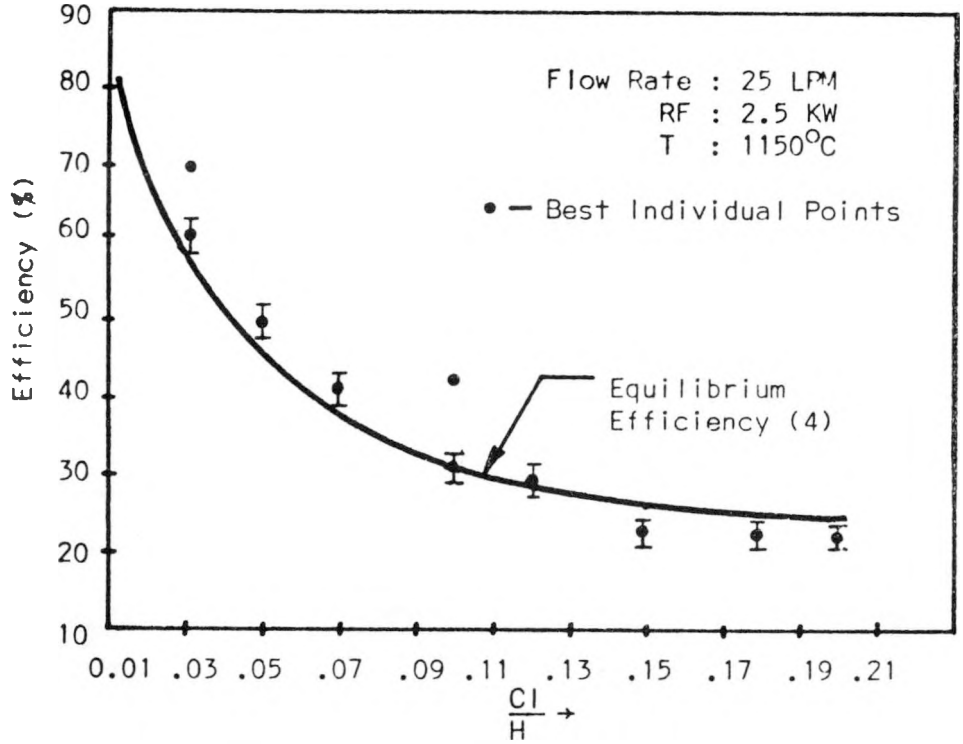

Figure 24: Effect of $SiHCl_3$ Concentration on Efficiency in Horizontal EBD.

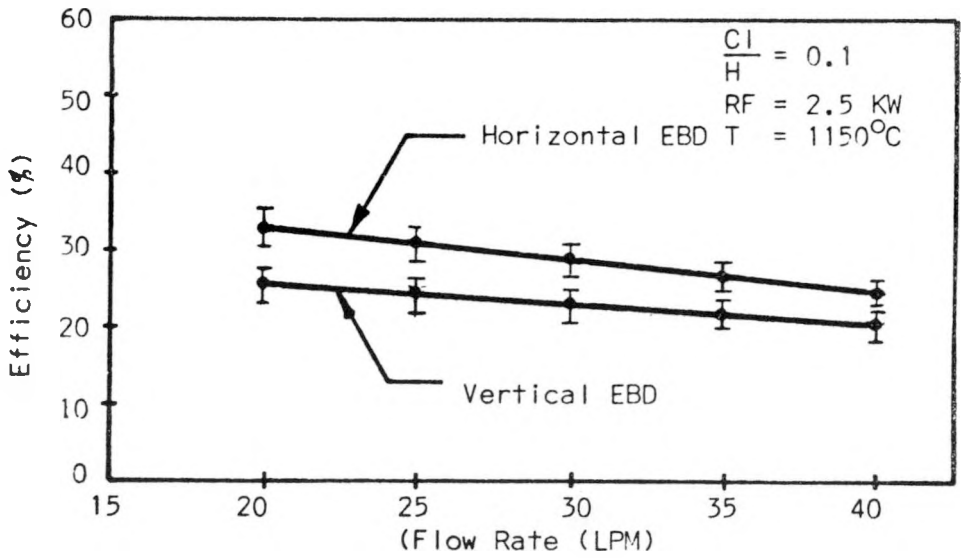

Figure 25: Effect of Flow Rate on Efficiency

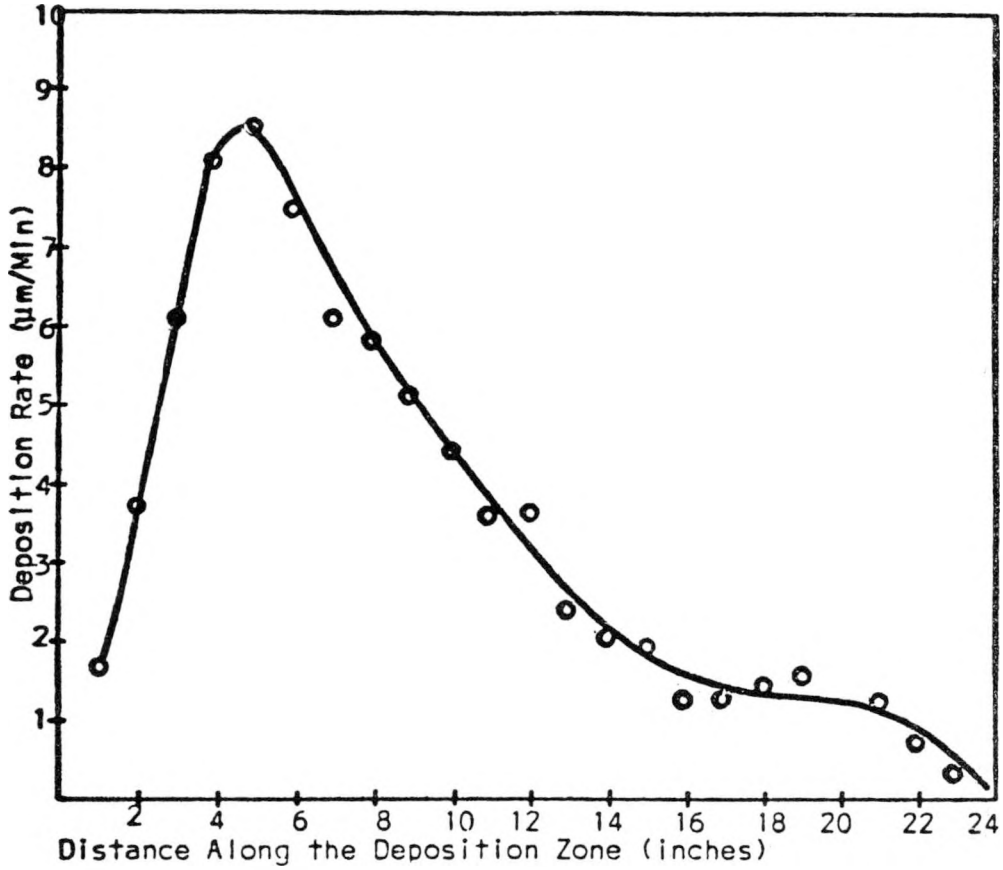

Figure 26: Typical Deposition Rate Variation Along the Center Line of the Substrate.

rapidly and reaches a maximum at about 5" from the beginning of the deposition zone, and then decreases. Maximum deposition rates of up to 16 μm/min. were realized in some experiments. This kind of deposition rate variation along the deposition zone is not detrimental to the production of uniformly thick silicon ribbons, since a continuous EBD system is envisioned to be the eventual mode of operation. In a continuous EBD system, the substrates will be translated through the deposition zone, which will average out the deposition rate, and silicon ribbons of uniform thickness will result. Deposition rate across the width of the substrates was found to vary slightly, indicating non-uniform mass transfer effects at the corners of the square cross-section reactor. This thickness variation across the width of the ribbon is sufficiently small that it does not affect the efficient use of this material for solar cell processing. The deposition rates on the bottom, side and top substrates in the horizontal EBD system were very similar and thus no definitive effects of gravity were observed in the horizontal system.

3.4 EFFICIENCY OF DEPOSITION

Even though chemical equilibrium calculations for a plasma temperature in the neighborhood of 4300K indicate (9) that over 95% of the input $SiHCl_3$ is reduced to silicon vapor for the concentration range shown in Figure 24, experimental EBD efficiencies are found to be strongly dependent on concentration. Furthermore, the average EBD efficiency is only a few percent different from what it calculates to be when complete equilibrium is established in the gas phase at the deposition temperature of 1150°C (the EBD efficiency being higher than the equilibrium efficiency for $\frac{Cl}{H} < 0.12$ and lower for $\frac{Cl}{H} > 0.12$, Figure 24). Gas phase nucleation and powder growth can partly account for the lower than expected efficiencies. Homogeneous nucleation of silicon and subsequent powder growth during EBD were inferred from the brown powdery deposits at the exit side of the deposition

chamber and exhaust pipe. Thus, lower than expected EBD efficiency values are partly due to small silicon particles being exhausted from the reactor instead of being incorporated into the growing silicon ribbon. The same phenomenon can explain why the deposition efficiencies in the vertical system are lower than in the horizontal system. In a vertical system in which the gases are introduced at the top and exhausted at the bottom, silicon particles (since their density is higher than that of the ambient gases), can travel through the deposition zone more quickly and thus suffer fewer collisions with the substrate surface. This will result in more of the silicon particles being exhausted from the reactor, thus resulting in lower efficiency than in a horizontal EBD system.

An important factor that determines the deposition efficiency using a high temperature plasma is the rapidity with which the plasma is quenched to a low temperature (11,12). For example, in hydrogen reduction of Ta_2O_5 to produce Ta metal using a high temperature plasma jet, deposition efficiency was increased from 15% to 42% by decreasing the quenching distance from 5" to $\frac{1}{2}$" (12). Similar results were reported in the reduction of other refractory metal oxides such as WO_3. We have obtained similar results in some preliminary experiments involving gas chromatographic (GC) analysis of the exhaust gases from the EBD reactor. Regular EBD runs were conducted, except that the furnace was not used to heat the substrates. Deposition efficiency was calculated from the concentration of the exhaust gases determined by GC analysis. In the range of concentrations investigated ($0.04 \leq \frac{Cl}{H} \leq 0.1$), efficiencies in excess of 50% were observed. These studies will have to be continued to determine the effects of quenching on deposition efficiencies for higher $\frac{Cl}{H}$ ratios.

3.5 DEPOSIT CHARACTERIZATION

With the modified EBD systems, large area (up to 18" long and $1\frac{1}{2}$" wide) silicon ribbons have been produced as shown in Figures 27a and b. While macro-

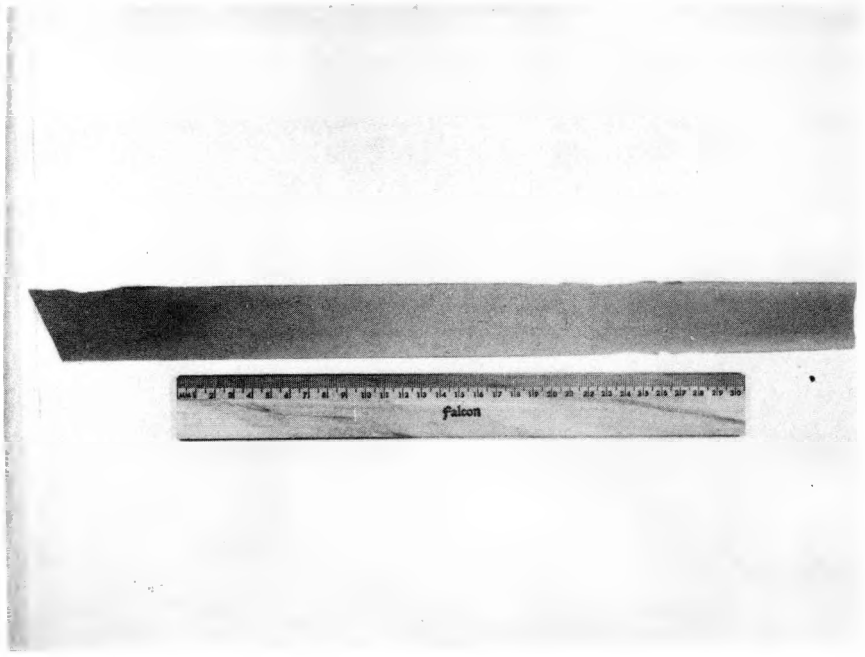

Figure 27a.

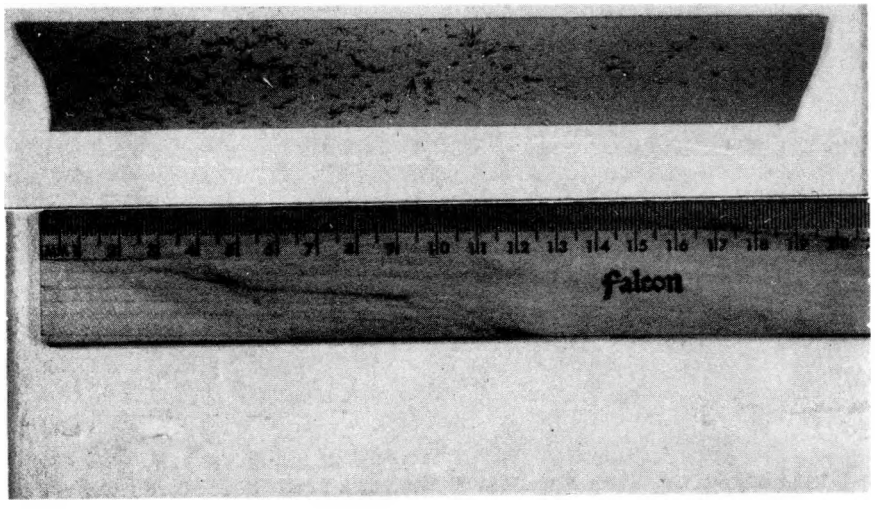

Figure 27b.

Figures 27a and b. Examples of Self-Supporting Silicon Films Produced Using the Modified Horizontal EBD System

scopically smooth silicon films (e.g. Figure 27a) were produced in some experiments, films of various surface morphologies (hillocks, whiskers, and nodules) resulted from other experiments (Figure 27b). Whiskers and nodules, when present, were more numerous in the beginning part of the deposition zone. The grain morphology of the silicon film in the beginning and latter parts of the depositon zone was also found to be slightly different, as shown in Figures 28 and 29. Figure 30 shows the area of a film containing whiskers and nodules. Most of the whiskers were found to be hexagonal in cross-section, and terminated with sharp (as well as hemispherical) tips. Figure 31 shows the normal view of a whisker terminating with a sharp tip. Figure 32 shows a high magnification photograph of a whisker terminating with an apparent hemispherical tip. Whisker branching can also be seen in this figure. The significance of the whisker tip morphology will be discussed later. Figures 33 and 34 show the cross-section of a silicon film containing an area where a whisker and a nodule have nucleated.

3.5.1 MECHANISMS OF WHISKERS AND NODULE GROWTH

Whisker formation during chemical vapor deposition has been studied in great detail. Initially whisker formation was explained on the basis of a screw dislocation mechanism. (13) In this theory, a screw dislocation terminating at a growth surface provides a self-perpetuating step. Accomodation of atoms at this step is energetically favorable, and is possible at much lower supersaturation than required for two-dimensional nucleation. Subsequent studies have indicated that not all whisker crystals contained an axial screw dislocation. Wagner et al. (14) have explained the growth of silicon whiskers on the basis of a vapor-liquid-solid (VLS) mechanism. The characteristics of this mechanism are that: (a) silicon whiskers do not contain an axial screw dislocation, (b) an impurity is essential for whisker growth, and (c) a small globule is present at the tip of the whisker during growth. Thus in the VLS mechanism an appropriate impurity forms a liquid

FIGURE 28: Surface Morphology of a Silicon Film from the Beginning Part of the Deposition Zone

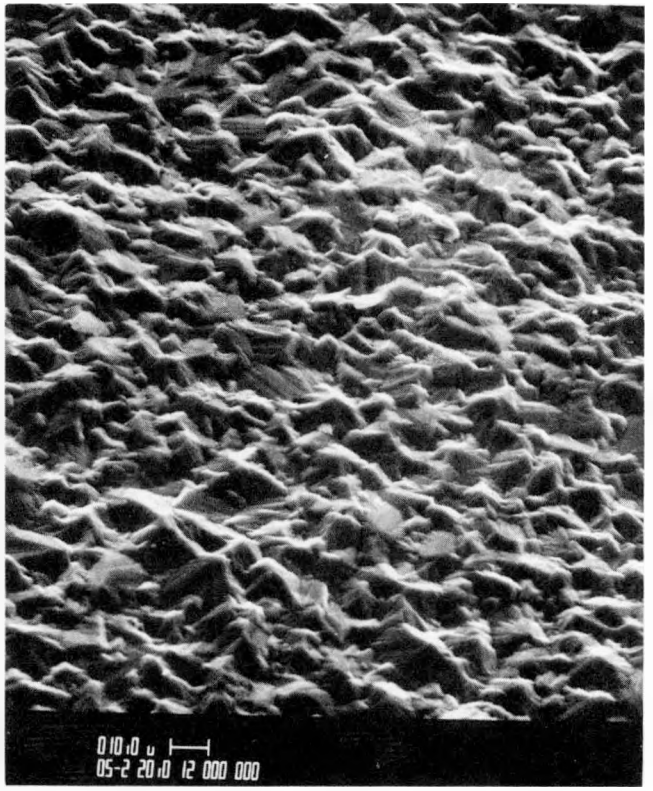

FIGURE 29: Surface Morphology of a Silicon Film from the Latter Part of the Deposition Zone

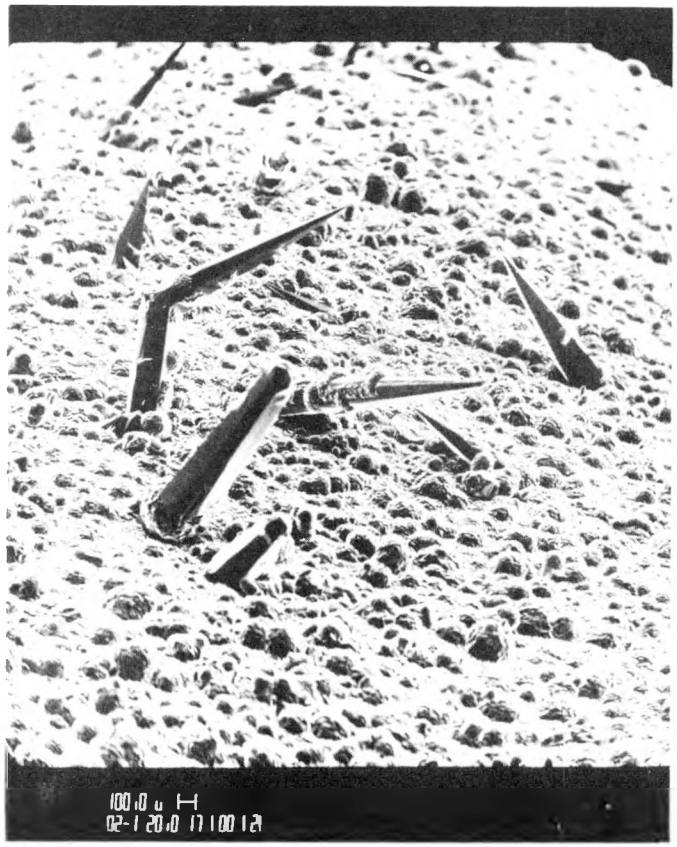

Figure 30. SEM Photograph of a Silicon Film Containing Nodules and Whiskers

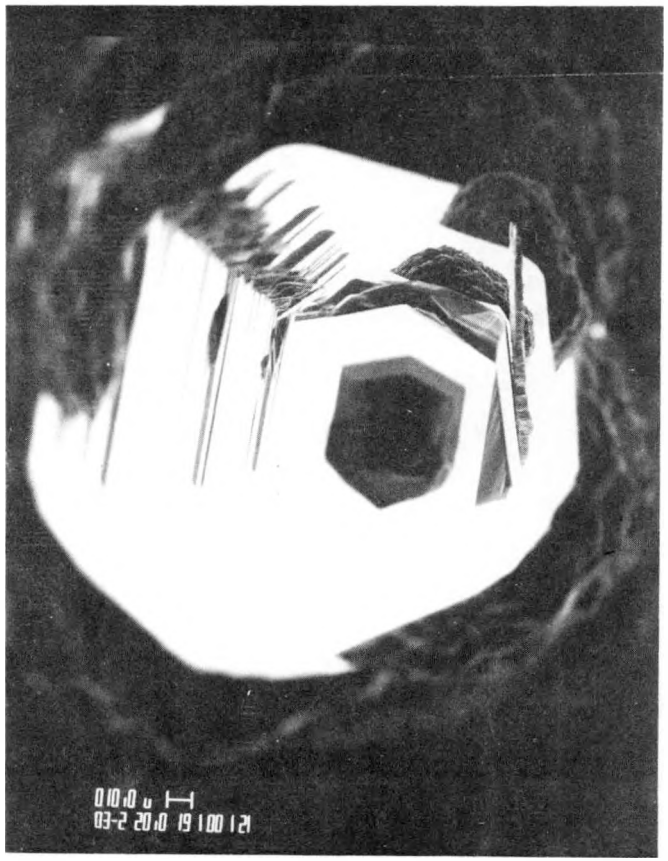

Figure 31. SEM Photograph of a Whisker Obtained While Viewing Along the Whisker Axis

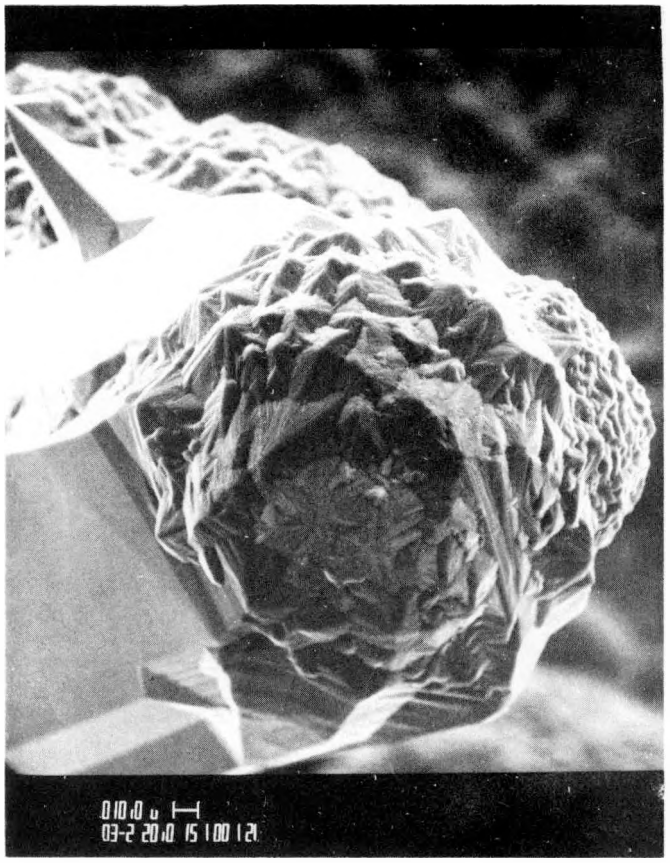

Figure 32. SEM Photograph of an Apparent Globular Whisker Tip

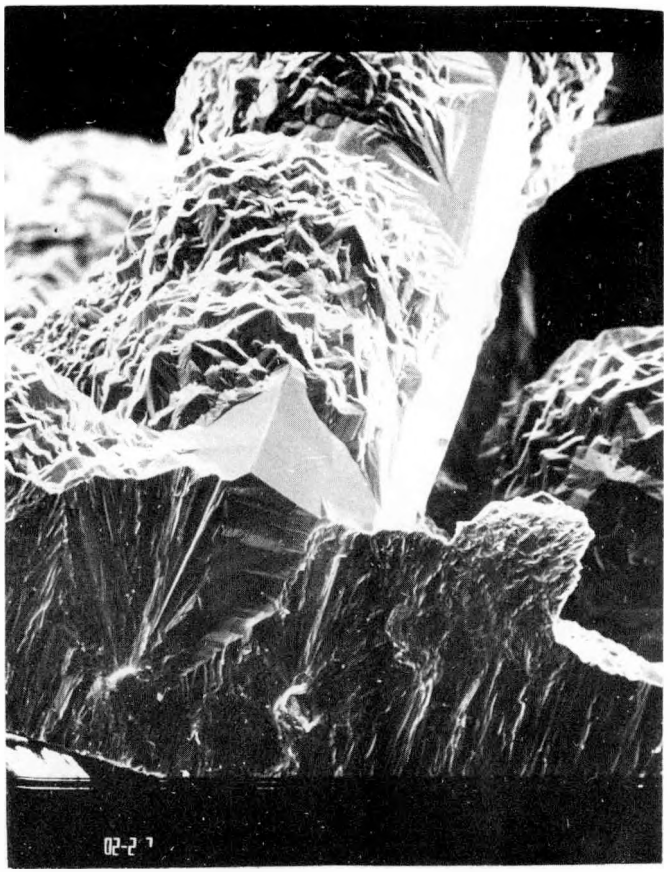

Figure 33. SEM Photograph of a Cross-Section of a Silicon Film Containing an Area Where a Whisker Has Nucleated

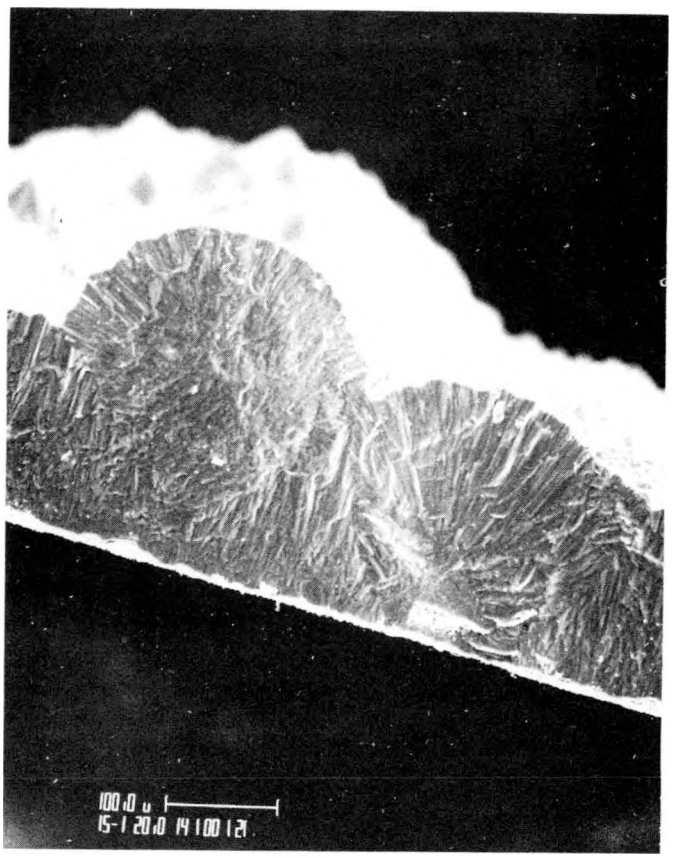

Figure 34. SEM Photograph of a Cross-Section of a Silicon Film from an Area Where a Nodule Has Nucleated

solution with the material to be deposited. The solution serves as a preferred site for deposition from the vapor and hence the liquid becomes supersaturated. Crystal (whisker) growth occurs by precipitation from the supersaturated liquid at the solid-liquid interface. Wagner et al. have deliberately grown whiskers of silicon on single-crystal silicon substrates by introducing one of the impurities - Au, Ag, Pt, Pd, Cu and Ni. The growth direction of these whiskers was found to be either <111>, <110>, or <211>. Bootsma et al. (15) have found that the chemical surface reaction at the vapor-liquid interface is the rate-determining step in whisker growth of silicon with Au as the impurity. They determined the activation energy for silicon growth by the VLS process to be 11.9 Kcal/mol., while it is 15.5 Kcal/mol. for the vapor-solid (VS) process from growth rate measurements (which indicated the growth rate by the VLS process was approximately two orders of magnitude higher than by the VS process). An important constraint on temperature for whisker growth by the VLS mechanism is that growth conditions should either be isothermal, or the temperature gradient should be such that the liquid surface is hotter than the substrate surface. When the liquid surface is cooler than the substrate surface, conditions give rise to the phenomenon of temperature-gradient zone melting (TGZM), (16) in which the liquid moves toward the higher temperature. Thus, whiskers cannot be grown by the VLS technique using cold-wall CVD systems (e.g., RF and radiation heated systems).

In our case no other impurity (excepting B_2H_6) is intentionally introduced into the system during deposition. Boron, with its segregation coefficient k of 0.8, does not meet the requirement, $k<<1$, for whisker growth by the VLS mechanism. Furthermore, the whiskers in our case do not appear to be terminating with globular tips (see Figures 30, 31, and 32).

Mendelson (17) has also observed whisker growth on some single-crystal silicon substrates during chemical vapor deposition with hydrogen reduction of $SiCl_4$. In his case the whiskers were always associated with the nucleation of tripyramids,

and hence he explained whisker growth by a re-entrant twin mechanism similar to that found for dendritic and ribbon growth of semiconductor materials (18).

Hillock (short whisker) growth has been observed due to stress relief in thin polycrystalline films (19) on substrates. The stresses can originate from defects generated during growth of a film (growth stresses), from lattice mismatch at the interface between substrate and film, and from differential thermal expansion. Chaudhari (19) has proposed that hillock growth is a form of stress relaxation in which atoms diffuse along the film-substrate interface to the base of the hillock. The latter extrudes out along the grain boundaries, connecting them to the rest of the film. Grain-boundary sliding and diffusion creep were found to play a dominant role in the growth of hillocks by the stress-relaxation mechanism. Once nucleated, these hillocks can grow much faster than the rest of the film due to the higher level supersaturation they are exposed to, compared to the rest of the film. Hillock nucleation (and growth) in our case requires that the silicon film be under compression (tension in the silicon film will lead to dip (crater) formation during deposition). This can happen if the temperature drops after the initiation of deposition, because the thermal expansion coefficient of silicon is smaller than that of Mo and $MoSi_2$ ($\alpha_{Si} < \alpha_{Mo} < \alpha_{MoSi_2}$), as can be seen in Figure 35.

We have examined the whisker tips and nodules by electron probe x-ray micro-analysis, and detected no impurities. This certainly rules out the VLS mechanism for whisker growth in EBD. The stress relief mechanism also does not appear to be responsible for whisker growth in EBD. As we have discussed earlier (see Section 3.2) the substrate temperature change after the initiation of deposition is so small (substrate temperature increases by about $15^{o}C$), that it can not generate a stress high enough to cause silicon to flow. Furthermore, the increase in temperature would put the silicon in tension rather than in compression, which is a basic requirement for hillock growth by stress relaxation mechanism.

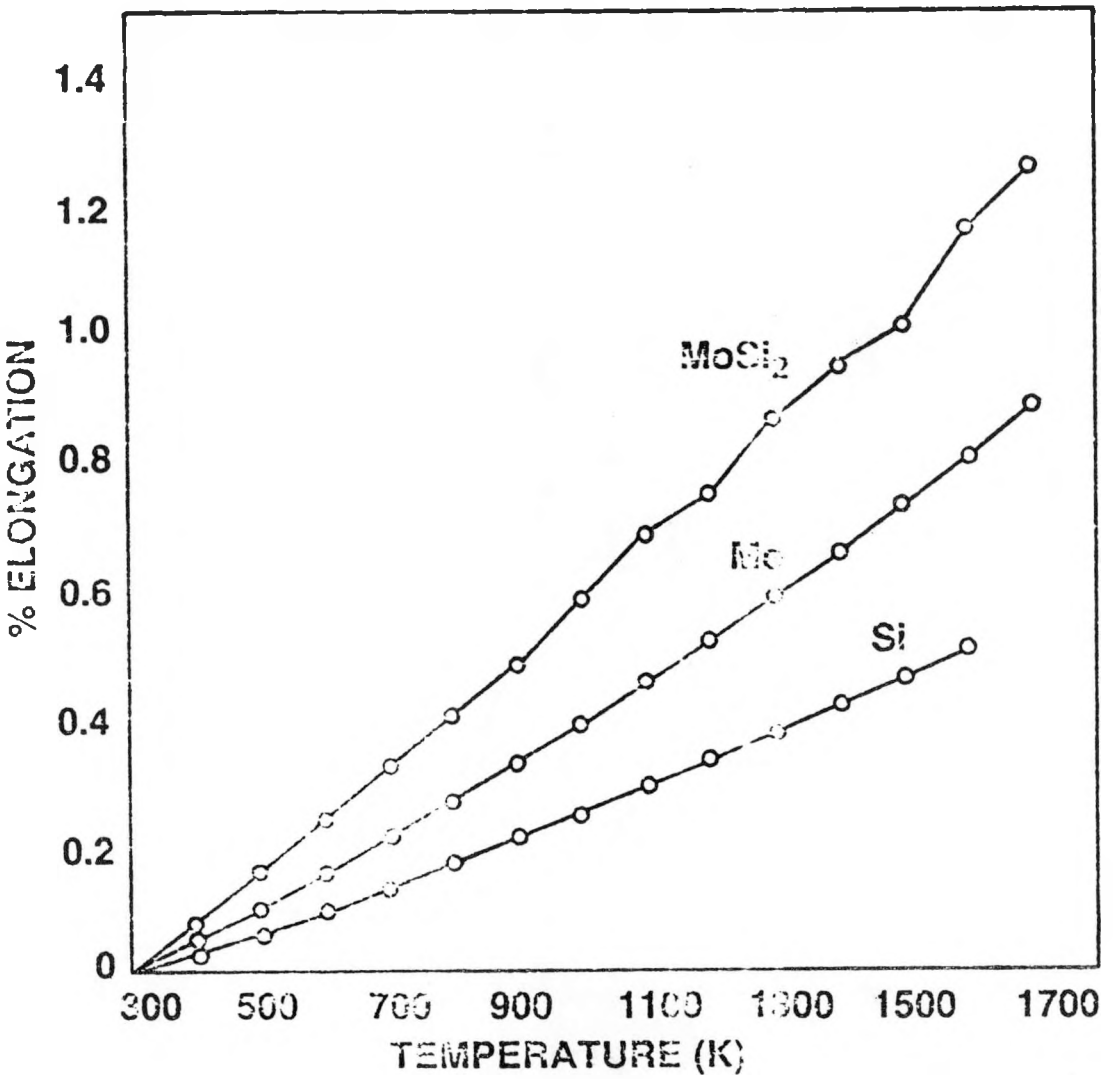

FIGURE 35: THERMAL EXPANSION DATA FOR Si, Mo AND $MoSi_2$ (FROM HANDBOOK OF THERMOPHYSICIAL PROPERTIES OF SOLID STATE MATERIALS, EDS. ALEXANDER GOLDSMITH ET. AL., PERGAMON PRESS (1962).

The deposition chamber geometry appears to influence whisker and nodule growth in EBD. When a square cross-section reactor (with a circular expanded entry section to minimize the propensity for beam arcing) was employed, numerous whiskers and nodules almost always resulted. With a circular cross-section reactor (with a circular expanded part for minimizing beam arcing), nodule and whisker density was dramatically reduced. When deposition was conducted with a rotating nozzle (see next section) in a circular cross-section reactor, a few nodules were observed, but whiskers were totally absent.

When using a deposition chamber with an expanded portion (for arc minimization), a brown powdery silicon deposits at the neck of the expanded portion of the quartz chamber. We believe that a major operating mechanism for whisker and nodule growth during EBD is by dislodgement of these powdery silicon particles (by the flowing reactant gas stream) and their subsequent landing on the dense silicon film growing on the Mo substrates. When the particles land on the growing silicon film with a favorable orientation, whisker growth can occur by a self-perpetuating re-entrant twin mechanism. When orientation is not favorable, these particles result in nodular growth. The substantial difference in density of nodules and whiskers in the silicon films obtained from square and circular cross-section reactors is due to the fact that particles from the deposit at the expanded neck of the square cross-section reactor can be dislodged more easily than those in the neck of the round cross-section reactor. In the deposition experiments with a rotating nozzle, this situation (powdery deposit and subsequent dislodgement of particles) did not occur.

To verify that this re-entrant twin mechanism is indeed responsible for whisker growth in EBD, we have examined the cross-sections of numerous whiskers. All the whiskers examined were found to contain twin planes as shown in Figure 36, confirming the twin mechanisms for whisker growth. The growth direction of the whisker shown in Figure 36 can be inferred to be <110> from the 2-fold symmetry.

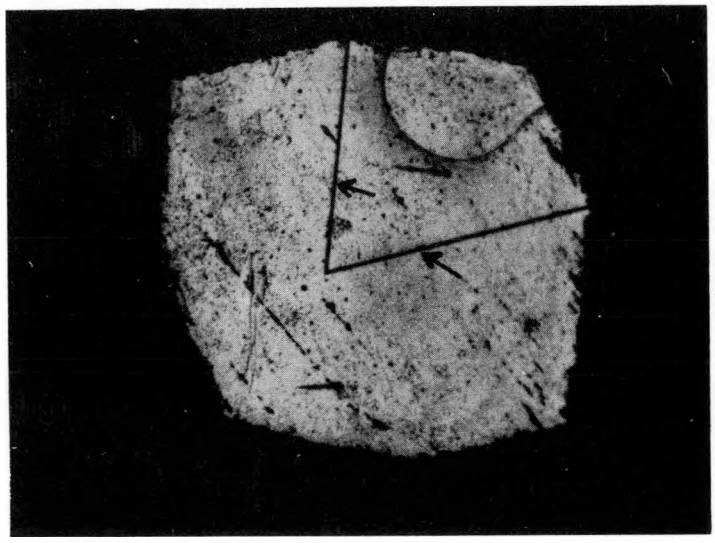

FIGURE 36: CROSS-SECTIONAL VIEW OF A WHISKER SHOWING THE TWIN PLANES. OTHER FEATURES IN THE MICROGRAPH ARE POLISHING AND ETCHING ARTIFACTS.

The two (111) twin planes are intersecting at an angle of 70° 32'.

It will be shown later that whiskers and nodules melt easily and become part of the silicon ribbon during laser recrystallization.

3.6 PLASMA GEOMETRY

To find an effective solution to the beam arcing problem (9), we have further investigated and developed alternate nozzle geometries. Utilizing an expanded portion in the deposition chamber near the nozzle for arc minimization is only a temporary solution because it could not be applied to a continuous EBD system which is considered the eventual mode of operation.

The multiple electrode (plasma) nozzle has been described in detail in reference (9). This nozzle was tested extensively during the initial part of the year. When it was operated close to arcing conditions (higher RF powers and shorter electrode-to-reactor wall distances), there was a tendency for one of the beams to arc and predominate, while the other beams lost power and got extinguished; this leads to the same problems associated with a regular nozzle. Thus with the multiple electrode nozzle, use of a 2" diameter reactor will invariably lead to arcing, however a 5" diameter reactor will not. Hence, because of the practical difficulties in routinely performing deposition experiments in a large EBD system (perhaps producing 5" wide silicon films), we decided to discontinue using the multiple electrode nozzle, until the deposition system gets scaled up to produce very wide silicon films.

The basic principle of another nozzle geometry - the rotating nozzle - has been described in reference (9). This rotating nozzle employs an eccentrically mounted electrode and is rotated during deposition, which results in the electrode being closer to different points of the substrates during rotation. Thus the plasma beam will be rotating inside the reactor, changing its point of attachment to the

substrates, which eliminates the problems of a local hot spot (arc). The principle of a rotating nozzle was verified easily; however, considerable developmental effort was expended in improving designs and minimizing impedance matching problems. Table 5 summarizes the list of typical experiments conducted using the rotating nozzle.

The initial rotating nozzle design was described in detail in reference 20. In this design, nozzle rotation is accomplished with a Doublin rotating union with a motor and pulley assembly. The output tube of the impedance matching network was soldered to the fixed end of the rotating union, while the nozzle with eccentric electrode was coupled to the rotating side of the union. The eccentricity of the electrode was brought about by mounting it at a 15^{o} angle to the axis of the nozzle. The plasma beam was successfully rotated during silicon deposition runs and silicon ribbons free of nodules and whiskers were produced. However, because of the closeness of the electrode to the substrates (distance between electrode and substrates was less than 1 cm) dense silicon was deposited on the electrode as well as the boron nitride shield. To eliminate (minimize) deposition on the nozzle, a new nozzle with reduced electrode eccentricity was fabricated. In this nozzle, the electrode was mounted at a 7^{o} angle. This electrode has an eccentricity of about $\frac{1}{2}$". As expected, silicon deposition on the electrode and nozzle was reduced. Next, to make the rotating nozzle suitable for a continual EBD system capable of producing silicon ribbons up to 24" in length, the length of the output tube was increased. This caused problems in impedance matching and thus initiating the electrical discharge plasma. The impedance matching problems were somewhat reduced when the massive, conducting feed-through was replaced by a high dielectric strength elastomer (spring loaded) dynamic seal (obtained from Fluorocarbon Co., Los Alamitos, California 90720). The seal retainer was made of Macor (trade name of Corning for a machinable glass

TABLE 5: SUMMARY OF TYPICAL EBD EXPERIMENTS USING ROTATING NOZZLE

NO.	RUN NO.	ROTATING NOZZLE DETAILS	GAS FLOWS (LPM) PLASMA	SHEATH	RF POWER (KW)	SUBSTRATE TEMP. ^{o}C	RUN TIME (MIN.)	RESULTS AND COMMENTS
1	H-77	Dublin rotating union and feed-through, electrode mounted at 15°C, 120 rpm rotation	H_2=16.0 B_2H_6=0.2 (a)	H_2=8.3 $SiHCl_3$= 10 gpm (b)	2.0	1100	30	The beam rotated all during deposition The resulting silicon ribbons were completely free of nodules and whiskers. Because of the closeness (<1cm) of the substrate and electrode, lot of dense silicon deposited on the electrode and BN shield.
2	H-104	Doublin rotating union and feed-through, electrode mounted at 7°, 60 rpm rotation	H_2=25.0 B_2H_6=0.24	H_2=8.0 $SiHCl_3$= 10 gpm	3.0	1150	60	Impedance matching problems experienced. Silicon deposition on the electrode and BN shield were reduced. Silicon ribbons free of whiskers and nodules were produced.
3	---	Same as above but increased the length of the output tube for using it with continuous EBD system.	H_2=16.0 B_2H_6=0.2	H_2=8.3	2.0	---	--	Electrical discharge could not be initiated due to severe impedance matching problems.
4	---	Same as above but for replacing the Doublin with an elastomer rotating seal.	H_2=16.0 B_2H_6=0.2	H_2=8.3	2.0	---	--	Impedance mismatch was reduced enough to initiate a hydrogen plasma. However, when $SiHCl_3$ is introduced, plasma was extinguished.
5	---	Same as above but changed the inductor in the impedance matching module. 60 rpm rotation.	H_2=16.0 B_2H_6=0.2	H_2=8.3 $SiHCl_3$= 10 gpm	2.0	---	30	Impedance mismatching was dramatically reduced. Stable plasma beam was obtained and it rotated all during testing.

a: B_2H_6 was 10 ppm in H_2
b: gpm - grams per minute.

ceramic with a high dielectric strength) to minimize the potential for arcing near the seal. A schematic of the modified rotating nozzle assembly is shown in the Figure 37. By changing the inductor in the Pi network of the impedance matching module, the impedance mismatch was dramatically reduced (12). A stable plasma beam was successfully rotated under actual silicon deposition conditions after these modifications. This nozzle should still be further evaluated in the continual EBD system.

3.7 CONTINUAL ENERGY BEAM DEPOSITION (EBD)

A continual EBD system eliminates some of the fundamental limitations of a batch EBD system (such as thickness variation along the length of the ribbon) and improves the economics of the process. During this year we have designed and constructed a preliminary version of a continual (moving substrate) EBD system. All the engineering drawings of this system were included in reference 21. This system was designed around a square cross-section (2" side) quartz reactor. Two inch wide silicon ribbons with lengths up to 24" can be produced using this system. While the molybdenum substrates translate on the bottom wall of the deposition chamber, the other three walls are covered with stationary Mo substrates to protect the quartz chamber from silicon deposition (and devitrification). Gas barriers at the entrance and exit sides of the reactor are comprised of two sets of nitrogen purge ports and a set of evacuation ports. The evacuation ports are connected to a rotary vacuum pump. For effectiveness of these gas barriers, the N_2 flow rate and evacuation rate have to be balanced. These in turn depend on the pressure inside the deposition chamber which is a function of the reactant gas flow rate. The bottom substrate transport mechanism consists of an Mo belt carrier, a motor, a speed controller at the take up reel and a pressure pad at the supply reel.

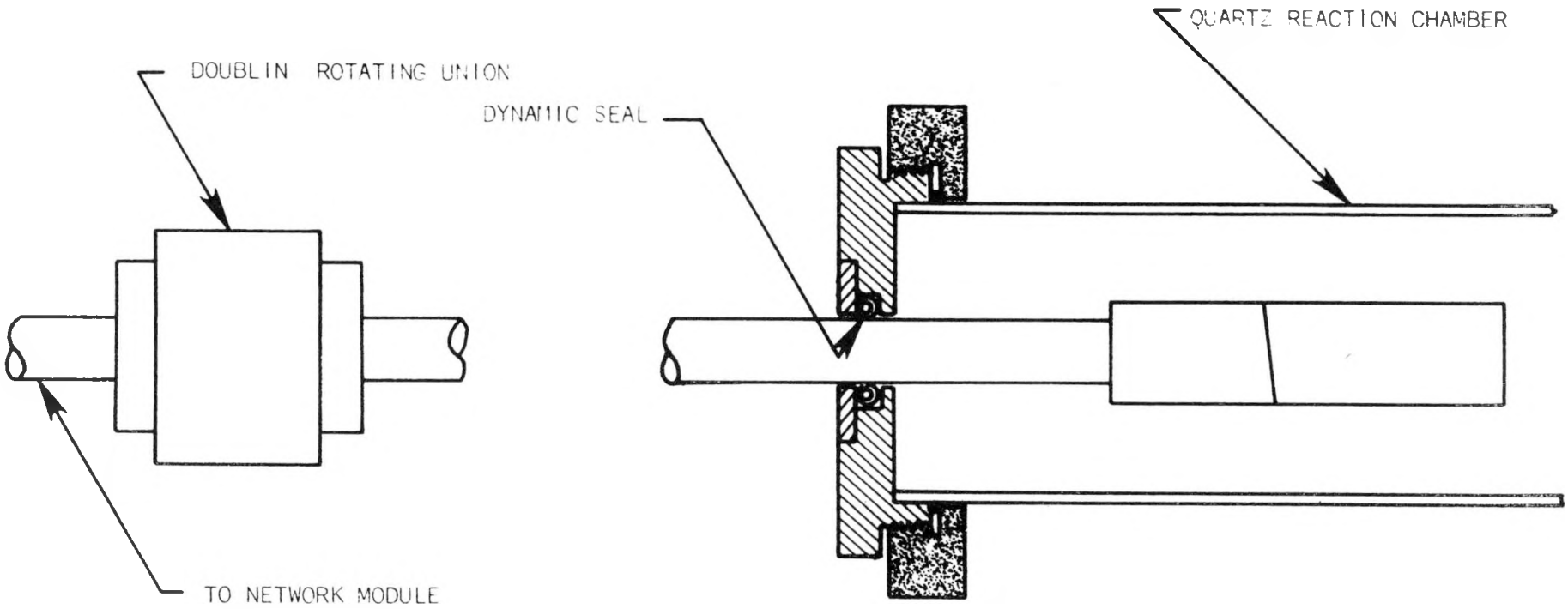

FIGURE 37: Modified Rotating Nozzle Assembly

Assembly was completed during the last quarter of this year. Figures 38 - 40 are photographs of this system. Figure 38 shows the network module with the nozzle rotation mechanism. Figure 39 shows the supply reel with a pressure pad and front panel controls for evacuation and purge port flows. Figure 40 shows the end view of the system with the clam-shell furnace open, showing the deposition chamber, gas barriers and the take-up reel for substrate transport.

Some initial experiments have been performed using the continual EBD system, and these are summarized in Table 6. Initially the system was operated in a CVD mode (without Energy Beam plasma) while the gas barriers and substrate translation mechanics were debugged. Figure 41 shows examples of ribbons produced in one run operated in a CVD mode. The average thickness of these ribbons was about 7 mils. The brown color on top of the ribbons was due to deposition of gas phase nucleated silicon particles. A run was also conducted using the Energy Beam. However, due to problems in operation of the rotating nozzle and the furnace, the run was aborted.

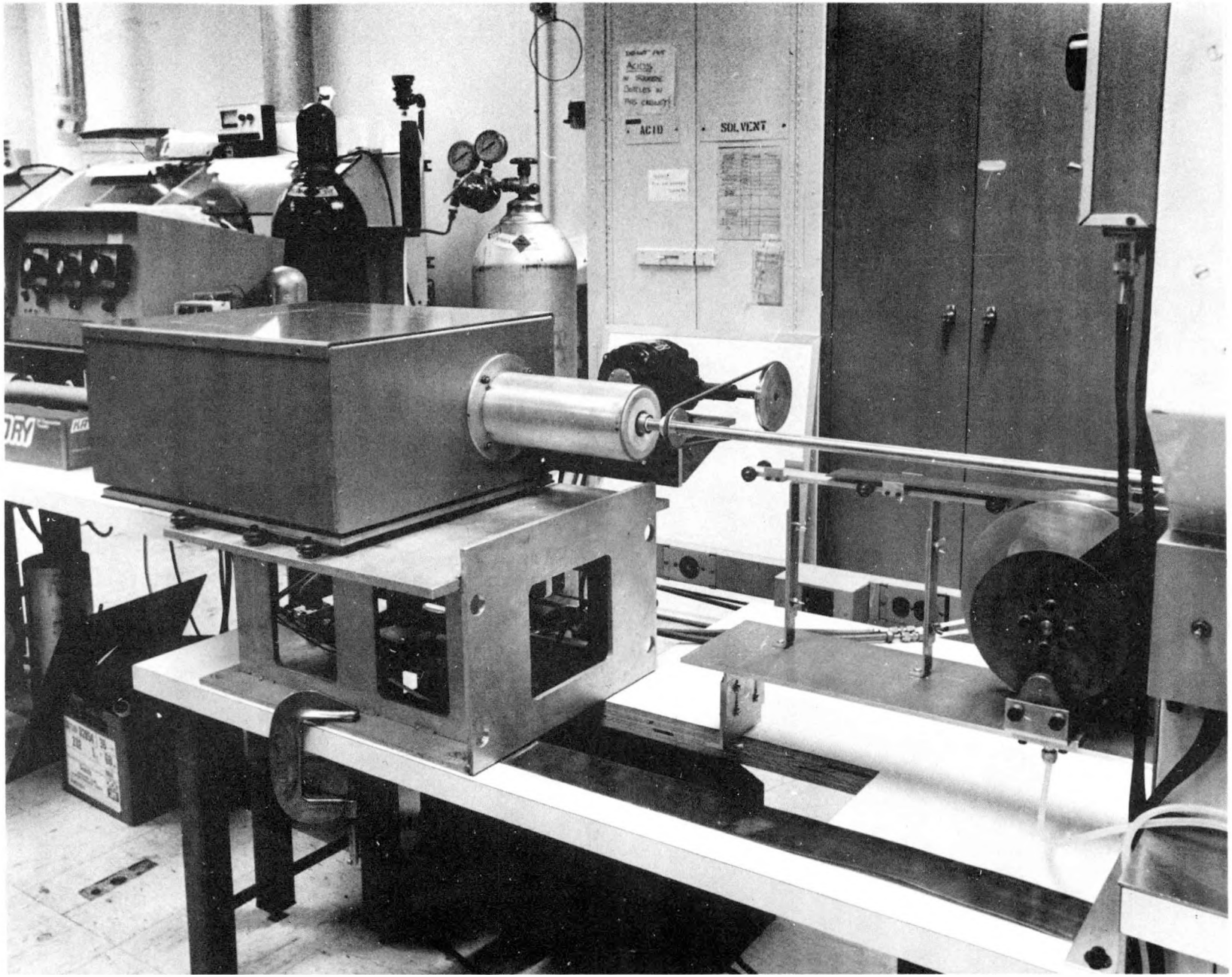

FIGURE 38: PHOTOGRAPH OF THE CONTINUAL EBD SYSTEM SHOWING THE NETWORK MODULE WITH THE NOZZLE ROTATION MECHANISM.

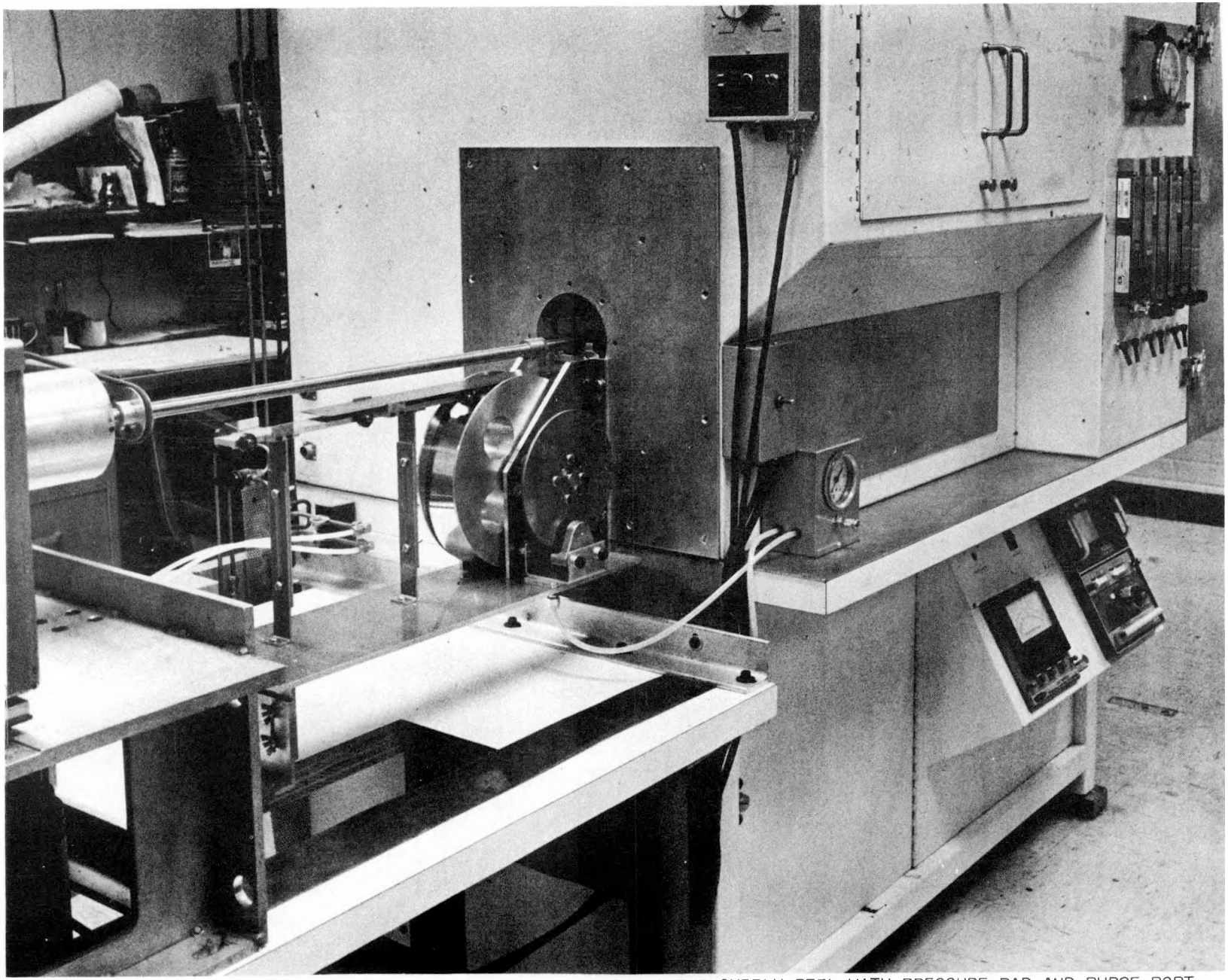

FIGURE 39: PHOTOGRAPH OF THE CONTINUAL EBD SYSTEM SHOWING THE SUPPLY REEL WITH PRESSURE PAD AND PURGE PORT FLOW CONTROLS.

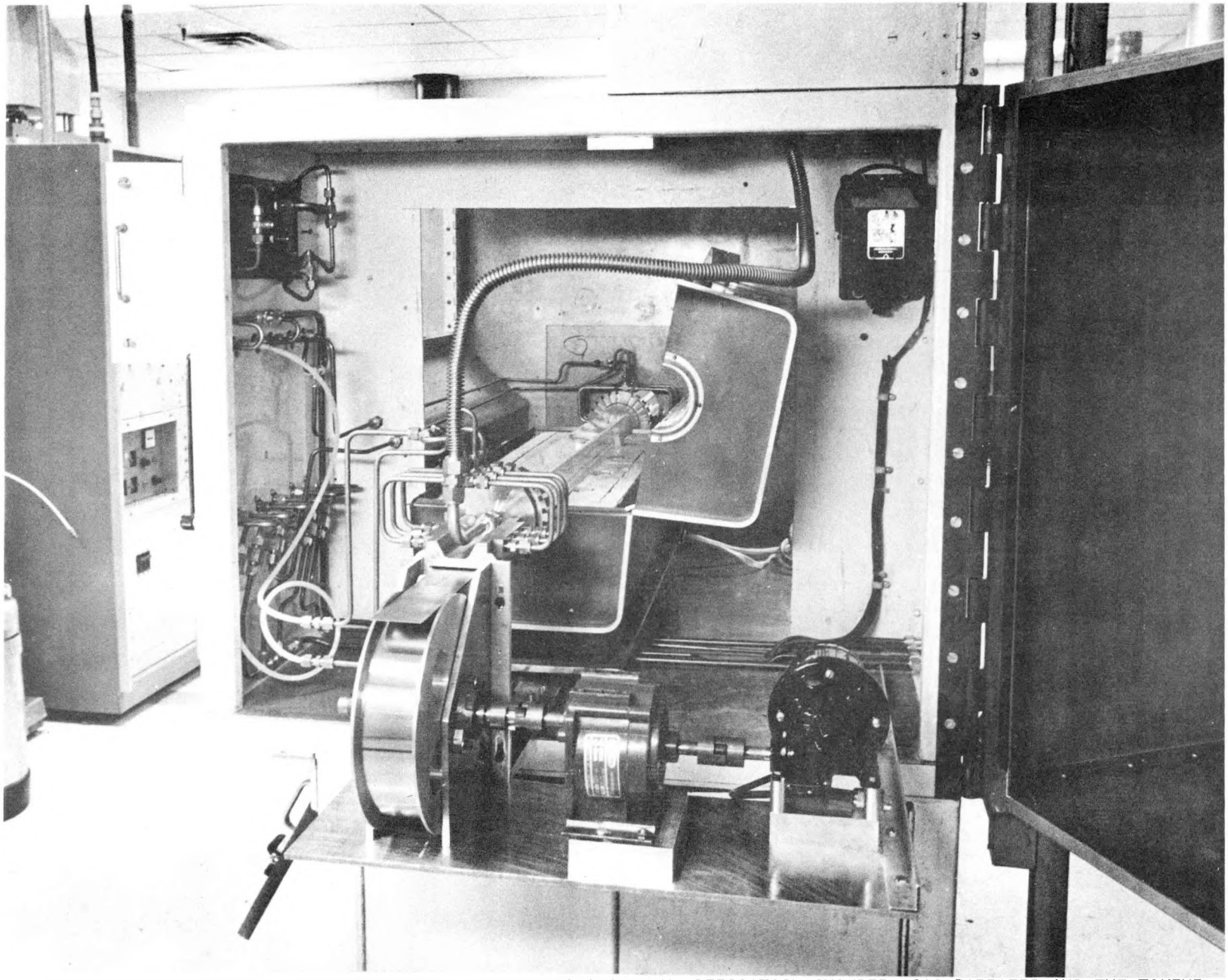

FIGURE 40: END VIEW OF THE CONTINUAL EBD SYSTEM, SHOWING THE DEPOSITION CHAMBER, GAS BARRIERS AND THE TAKEUP REAL FOR SUBSTRATE TRANSPORT.

TABLE 6
SUMMARY OF EXPERIMENTS IN CONTINUOUS ENERGY BEAM DEPOSITION (CEBD) SYSTEM

RUN NO.	CONDITIONS	GAS FLOWS (LPM) PLASMA	GAS FLOWS (LPM) SHEATH	SUBSTRATE TEMP. °C	RF POWER KW	BELT SPEED CM/MIN	RESULTS & COMMENTS
CEBD-1	The two sets of N_2 ports on the entrance and exit side controlled by a single flow meter.	H_2=8.0 B_2H_6=0.4	H_2=8.0 $SiHCl_3$=7.5 gpm	1200	CVD Mode	0.75	Problems with gas seals at high reactant flow rates, and the substrate translation mechanism. Broken pieces of separated silicon film resulted.
CEBD-2	Independent control of each set of N_2 ports, exhaust pipe changed to 1" dia. (from $\frac{1}{2}$" dia). Moly clips for improving substrate transport.	H_2=15.0 B_2H_6=1.0	H_2=15.0 $SiHCl_3$=15gpm	1200	CVD Mode	0.75	Exit side port size not enough for passage of substrate with silicon film without breakage. Broken silicon ribbons resulted.
CEBD-3	Same as in CEBD-2 excepting that a 1/8" high exit purge port is replaced with a $\frac{1}{4}$" high purge port	H_2=15.0 B_2H_6=1.0	H_2=10 $SiHCl_3$=12gpm	1200	CVD Mode	1.0	About 10 silicon ribbons were produced. All without breakage. Average thickness 7 mils.
CEBD-4	Same as CEBD-3, with Energy Beam.	H_2=15.0 B_2H_6=1.0	H_2=10 $SiHCl_3$=12gpm	1200	2.0	1.0	Front zone of the furnace failed. Beam arcing after 30 minutes of run to a localized spot. Run discontinued.

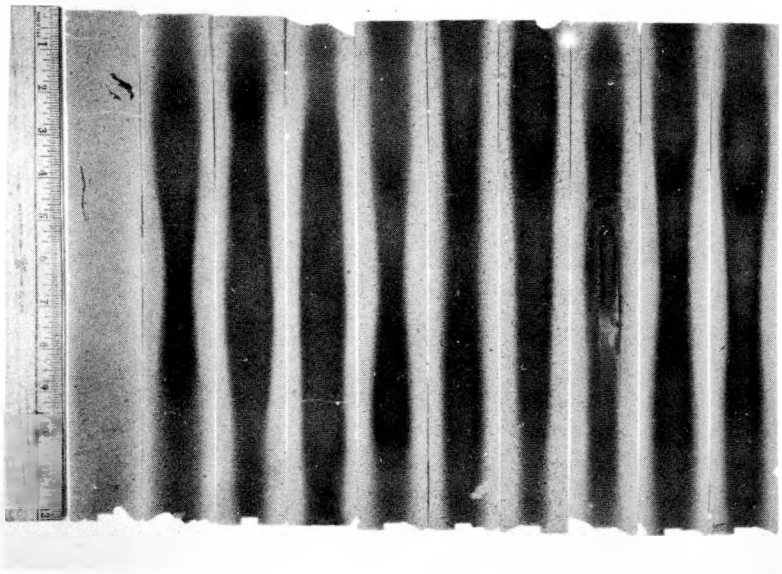

FIGURE 41: EXAMPLES OF SILICON RIBBONS PRODUCED IN ONE RUN IN THE CONTINUOUS ENERGY BEAM DEPOSITION (CEBD) SYSTEM OERATED IN A CVD MODE.

4.0 GRAIN SIZE ENHANCEMENT AND CHARACTERIZATION

4.1 GRAIN SIZE ENHANCEMENT

As-deposited (and shear separated) silicon ribbons were grain enhanced by the conventional RTR laser recrystallization process. Initially some contamination problems were experienced (20) during the recrystallization process; these resulted in low minority carrier diffusion lengths in the ribbons and low solar cell efficiencies. However, the source of contamination was subsequently identified and eliminated, and high efficiency solar cells were fabricated.

Using the conventional RTR process, we could grain enhance finite length microcrystalline silicon ribbons only in their center sections because of the space taken by the profile furnaces (preheater and post heater).

Accordingly, we used a new RTR recrystallization procedure for finite length ribbons. This procedure increases the grain size in finite length separated silicon ribbons (produced in the batch EBD system and the "continual" EBD system) except for a thin peripheral region. We define a "continual" EBD system as one in which finite length substrates are moved through the deposition zone one right behind the other to produce finite length (12" to 24" long) silicon ribbons. This is distinguished from a "continuous" EBD system which uses a belt substrate to produce silicon ribbons of semi- infinite length. (A continuous EBD system is believed to be a long term possibility based on developments in composite TESS substrates.)

In the conventional RTR process, the fine grain polycrystalline silicon ribbon is held at both ends and moved through the scanned laser source after establishing a thin full width molten zone. Because of the requirements for pre- and post-heaters (for high grain enhancement rates) the ends of the ribbon could not be

grain enhanced by the conventional RTR procedure. In the new procedure, the ribbon is not melted to the very edges. The unmelted solid edges support the molten zone and eliminate the requirement for holding the ribbon on both sides for transporting through the scanned laser. Thus for example, the ribbon can be held only at the bottom edge initially and transported through the scanned laser source. After the top edge comes out of the post heater, the ribbon is held at the top, and the bottom edge is released. Thus by this new procedure (named Rigid Edge Growth) almost the whole area of the ribbon can be grain enhanced.

This Rigid Edge procedure can be automated with a "Cassette Transport" as illustrated in Figure 42. The fine grain ribbons stacked in a cassette at the top are transported through the scanned laser source and the grain enhanced ribbons are collected in a cassette at the bottom. Figure 43 shows an example of a ribbon grain enhanced by the rigid edge procedure. The microstructure in this ribbon (excepting at the edge) is identical to that in a ribbon grain enhanced with a full width melt. However, very near the edges, the unmelted edges influence the grain size as shown in Figure 44. However, for large area (wider and longer ribbons, the area influenced by the rigid edges can be reduced to less than 5% of the total area.

Another point of concern in the grain enhancement of EBD silicon ribbon was the presence of nodules and whiskers. Even though their presence required development of special handling and clamping procedures, they were found to melt and become part of the ribbon, thus resulting in a uniform surface, as can be seen in Figure 45.

4.2 MICROSTRUCTURE

Microstructure of EBD ribbons after RTR grain enhancement was studied to a limited extent. Wright etching (60 ml HF:30mlHNO_3:30 ml 5M CrO_3:2 gm $Cu(NO_3)_2 \cdot 3H_2O$:60 ml HAc:6 ml H_2O solution) and optical microscopy were used for studying

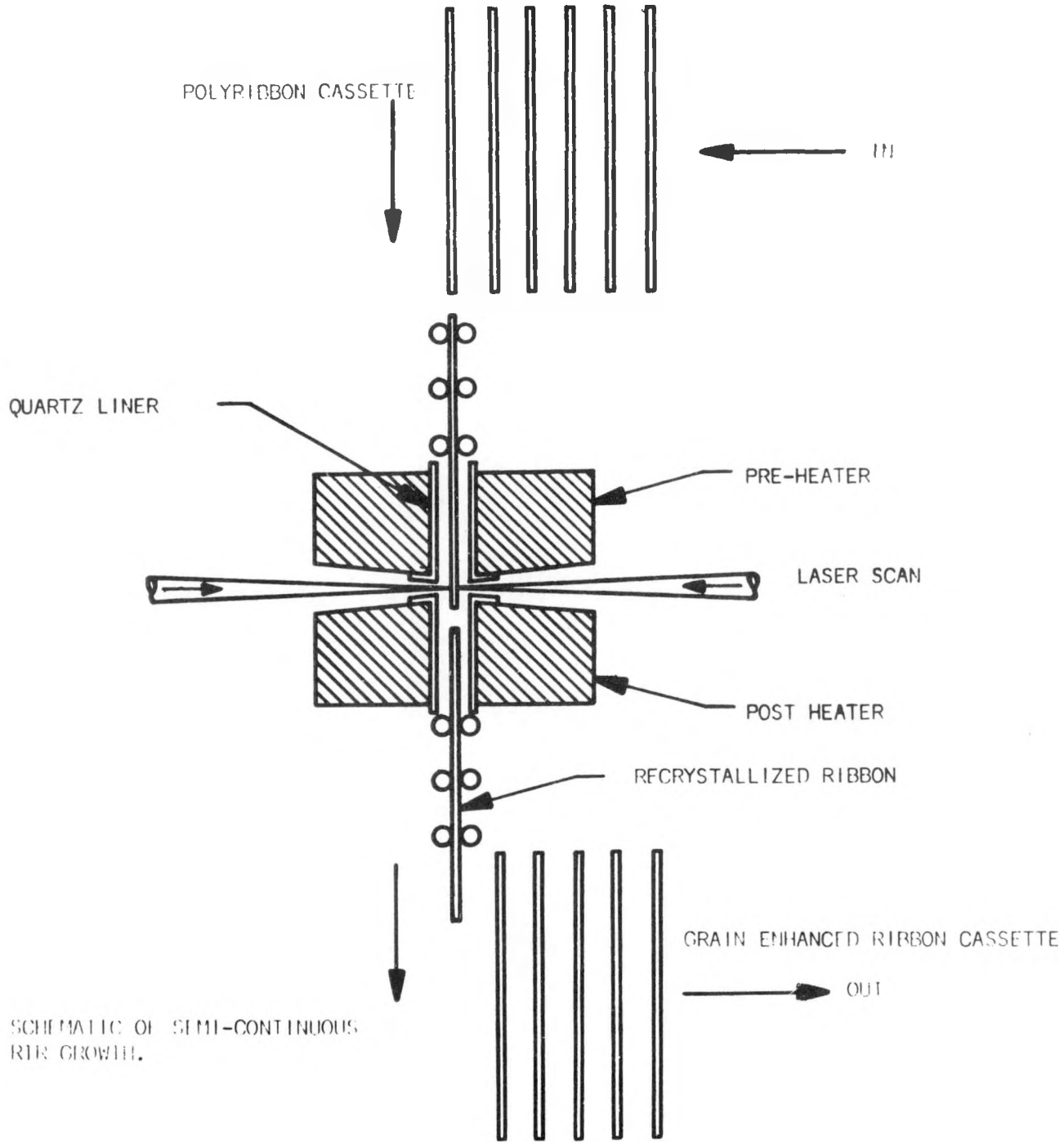

FIGURE 42: SCHEMATIC OF SEMI-CONTINUOUS RTR GROWTH.

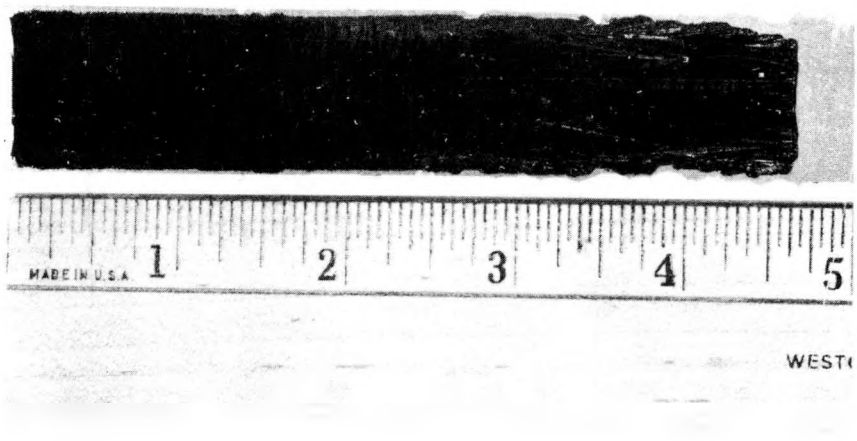

FIGURE 43: EXAMPLE OF A RIBBON GRAIN ENHANCED BY THE RIGID EDGE METHOD.

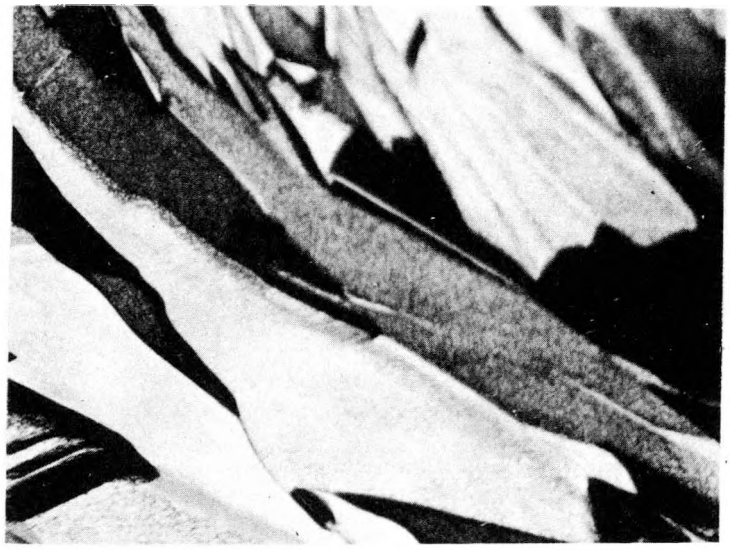

FIGURE 44: MICROSTRUCTURE NEAR THE RIGID EDGES IN THE RIBBON SHOWN IN FIGURE 43. 200X

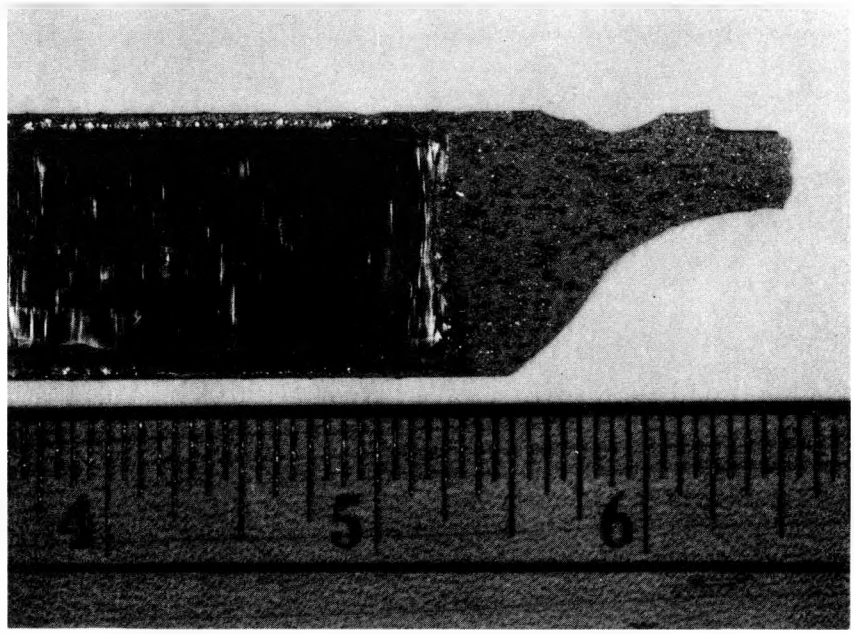

FIGURE 45: EXAMPLE OF AN EBD RIBBON CONTAINING NODULES AND WHISKERS, AFTER GRAIN ENHANCEMENT.

grain boundaries, twin boundaries, stacking faults and dislocation (etch pit) densities. The grains in these ribbons were found to be quite large - up to few mm wide and several cm long. They always extended through the thickness of the ribbon and thus no grain boundaries were observed parallel to the ribbon surface. Twin, stacking fault, and dislocation densities in these ribbons were found to be strongly dependent on the recrystallization process parameters such as post-heater temperature profile. A systematic study of the effects of the recrystallization process parameters on these defect densities is required to gain an increased understanding of the grain enhancement process.

Figure 46 is a photograph of a texture etched, recrystallized EBD silicon ribbon. Texture etching reveals the various grain orientations very strikingly. The grain selection process during recrystallization can be very easily seen in this ribbon. Presently, we are mapping orientations of the individual grains by the back reflection x-ray Laue technique to determine the preferred orientation(s) (growth directions).

4.3 ELECTRICAL PROPERTIES AND GETTERING

The resistivitiy of recrystallized EBD ribbons has been routinely measured by a four point probe and an RF conductance probe. Both techniques were found to be in good agreement. During this year we have produced and characterized only p-type (boron doped) silicon films. Minority Carrier diffusion length in grain enhanced ribbons was measured by the surface photovoltage (SPV) technique. The diffusion length in these grain enhanced ribbons was found to be in the 5 - 20 μm range indicating that a gettering step is necessary for improving the diffusion length for high efficiency solar cells.

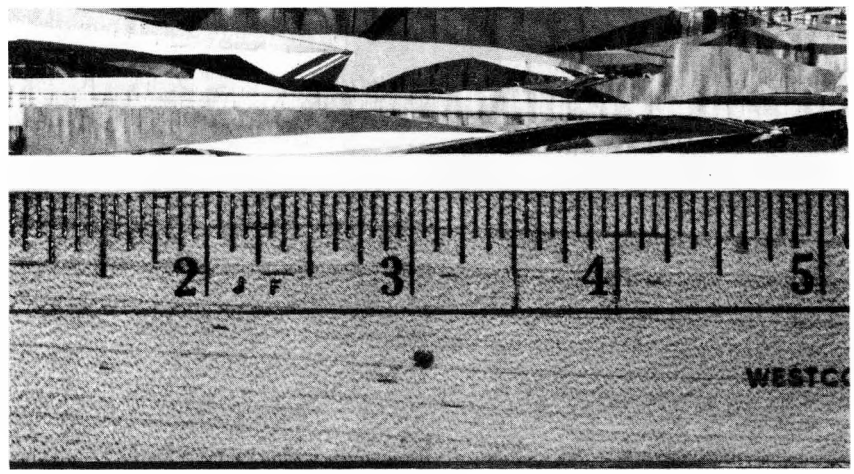

FIGURE 46: PHOTOGRAPH OF A TEXTURE ETCHED, RECRYSTALLIZED EBD SILICON RIBBON.

A double-sided phosphorus diffusion was found to getter these ribbons. Phosphorus was diffused from both sides of the ribbon at 900°C for 15 minutes to produce an n+-p-n+ structure. Then one of the n+ layers was etched off and diffusion lengths were measured by OCPV using the remaining n+-p junction as the barrier. Improvements in diffusion lengths up to 100 μm have been observed after this gettering process. Enhancements of minority carrier lifetime (diffusion length) in silicon by phosphorus diffusion has been well known (22,23). However, the various mechanisms involved in the gettering process and the types of impurities and/or defects that could be gettered are not completely known. We are planning to characterize this gettering process in our silicon ribbons.

5.0 SOLAR CELL PROCESSING AND EVALUATION

Solar cells have been fabricated on grain enhanced EBD films using the following processing sequence:

1. HF dip and rinse
2. Clean in $H_2SO_4 + H_2O_2$ at 120°C, rinse, Freon dry
3. Double sided PH_3 diffusion at 900°C for 18 minutes.
4. Establish a mesa pattern on one side by photoresist masking.
5. Etch both sides in a CF_4-O_2 plasma
6. Low pressure CVD (750°C, 30 min.) for an 850Å thick Si_3N_4 AR coating.
7. Open contact finger pattern in the Si_3N_4 by photoresist masking.
8. Metallize front and back by sequential Pd:Ag plating.

All the cells we have fabricated on this contract have been typically 1 cm x 2 cm as shown in Figure 47. Unless otherwise stated, all cells reported in this section have been pre-etched before grain enhancement to remove Mo contamination from the surface adjacent to the temporary substrate. The best cell fabricated to date had an efficiency of 10.06% under simulated AM1 illumination. Figure 48 shows the I-V characteristic of this cell.

The third step in the processing sequence not only provides an n+-p junction, but also getters the material, increasing the minority carrier diffusion length by as much as a factor of ten. By repetition of this getter cycle (i.e., diffuse, etch, diffuse, etch, diffuse), it was expected that an improvement in short circuit current would result over that seen in the singly gettered ribbons. This multiple gettering experiment was conducted on only a very limited number of samples to date, so the results should be considered tentative. Nevertheless, the best sample of this group had an efficiency of 9.4% with a J_{SC} of 26.3 mA/cm^2,

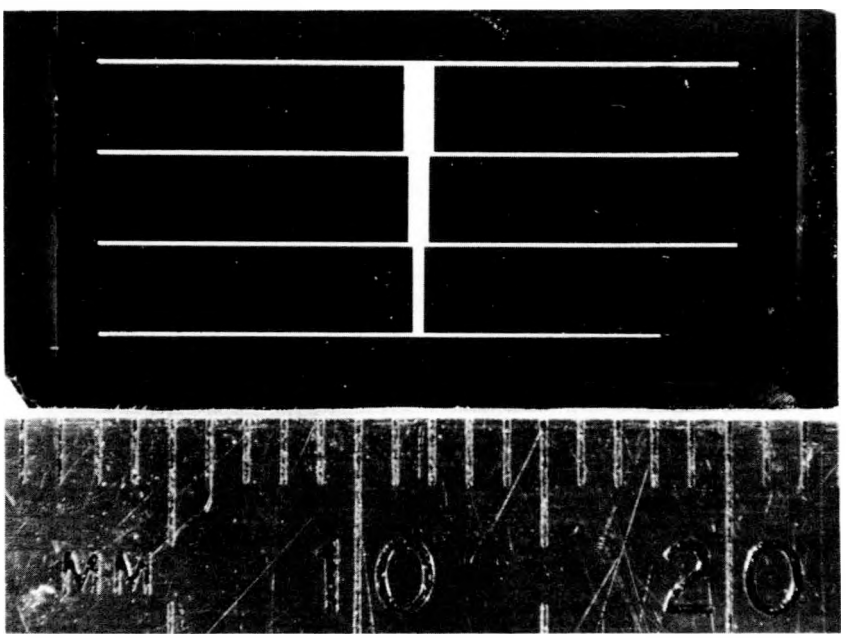

FIGURE 47: Photograph of a typical solar cell fabricated during this Program.

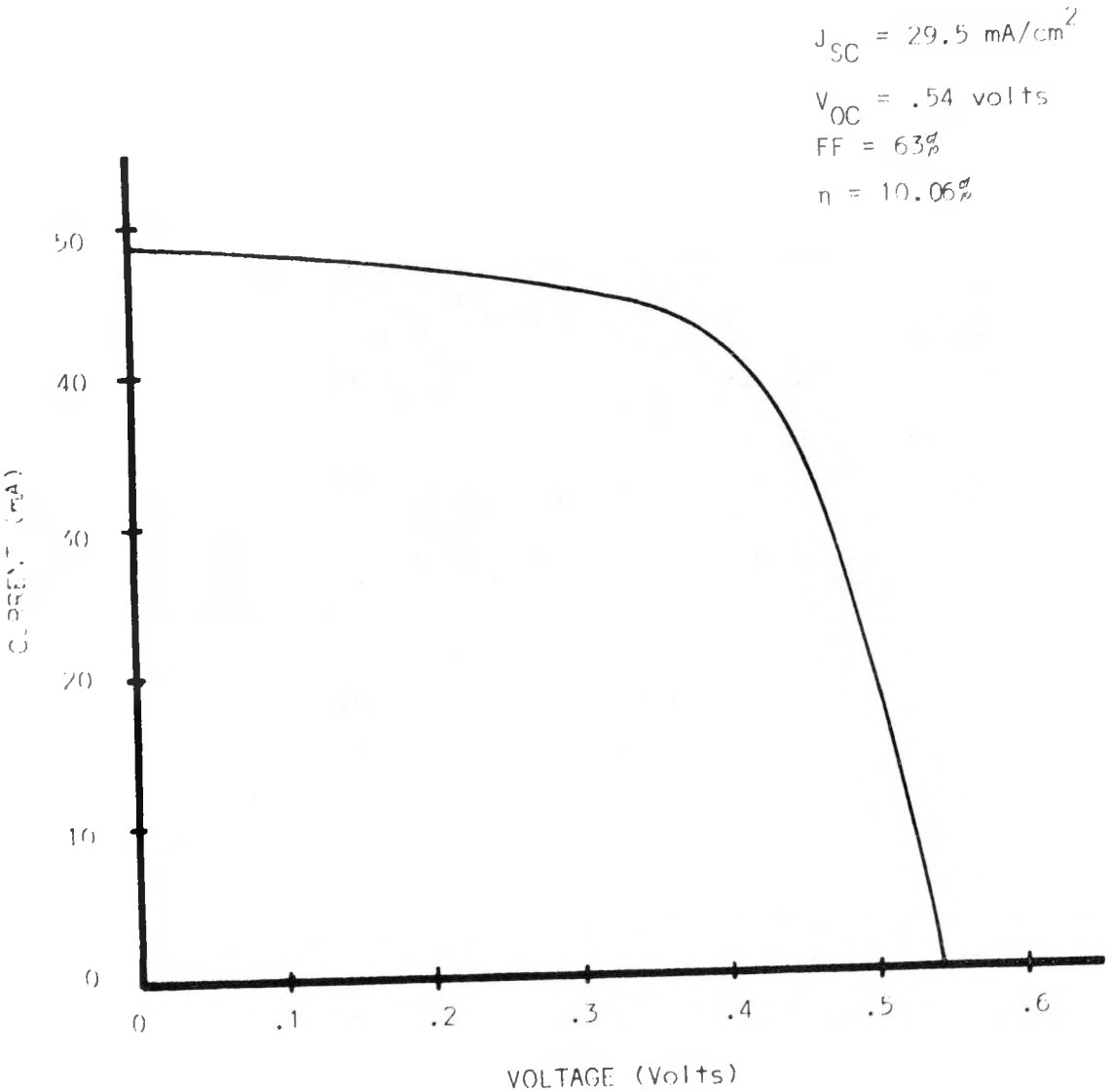

FIGURE 48: I-V characteristic of the cell 991A-1, under AM1 illumination.

V_{OC} of 0.56 and an FF of 64%. This would seem to indicate that the additional gettering cycles fail to provide any added benefit; however, a large number of cells will have to be processed and evaluated before a judgement could be made.

A study was also initiated to determine the effect of substrate temperature during EBD on the solar cell efficiency parameters. Table 7 shows the SPV diffusion length in the as-recrystallized samples as a function of substrate temperature during EBD. Contrary to expectations, diffusion length appeared to decrease as substrate temperature during deposition is decreased. Unfortunately, this group of ribbons was broken during cell fabrication, so data are limited. Hence further studies are required to completely evaluate the effects of substrate temperature during deposition.

Some experiments to determine the effects of base resistivity on solar cell efficiency were conducted. An attempt was made to fabricate solar cells on high (10 Ω-cm), medium (our standard 1 Ω-cm) and low (0.3 Ω-cm) resistivity ribbons. The ribbon that was doped to obtain a 10 Ω-cm resistivity, ended up varying in resistivity from 20 - 200 Ω-cm after grain enhancement, and was removed from further analysis. The low resistivity solar cells were lower in efficiency than the medium resistivity cells. The short circuit current was 10 - 20% lower, and the typical efficiency for the 0.3 Ω-cm cells was 7.5 - 8%. Probing of these cells prior to metallization indicated open circuit voltages as high as 0.600 volts, but after metallization, the highest reading was 0.56V. The reason for this is believed to be that, in pre-metal probing, only a small area in the vicinity of the metal probe is sampled. After metallization, all regions of the cell are electrically connected; this allows small but highly shunting regions to drag down performance of the entire cell. In these cells, the bad regions were found to be at one edge of the ribbon.

TABLE 7:

EFFECT OF SUBSTRATE TEMPERATURE DURING EBD ON MINORITY CARRIER DIFFUSION LENGTH IN THE SILICON RIBBON AFTER GRAIN ENHANCEMENT.

EBD TEMPERATURE (^{o}C)	DIFFUSION LENGTH (μM)
1050	9
1100	17
1125	20
1150	20

6.0 CONCLUSIONS AND RECOMMENDATIONS

Significant progress has been made in all tasks of this program during the year. Shear separation of silicon ribbon from TESS substrates was found to occur in the silicon ribbon very close to (within 100Å) the Si-$MoSi_2$ interface. The ppm level of Mo contamination on the back side of separated silicon films may be occurring from imperfect shear separation and/or from grain boundary diffusion of Mo through the $MoSi_2$ separation layer. Composite TESS substrate -- Mo (thick): SiO_2 (thin):Mo (thin) and thin Mo coated graphite and Al_2O_3 substrates show promise for substantial improvements in recyclability. Further work is needed in evaluating new TESS substrate configurations and developing the one that appears economically most attractive. The batch EBD systems have been optimized through parametric studies and large area (up to 1½" x 18") micro-crystalline silicon ribbons, have been routinely produced. Further work is needed to improve (assess) the deposition efficiency capability of the EBD process. A continual EBD system was designed, fabricated and underwent initial operation. This system should be optimized to produce quality microcrystalline silicon ribbons at high deposition efficiency and deposition rate.

Solar cells with efficiencies up to 10.1%, under simulated AM1 illumination, were fabricated on grain enhanced EBD silicon ribbons. Experiments have been initiated to determine the effects of various gettering parameters, substrate temperature during deposition, and base resistivity, on solar cell efficiency parameters.

Based on the results so far, it appears that by optimizing the Energy Beam deposition parmeters, and cell fabrication parameters, solar cell conversion efficiencies of up to 12% should be feasible. No apparent degradation has been observed in these cells. The economic analysis of this process; using Mo temporary substrates, that we reported in the previous annual report (9) still appears valid. This analysis has indicated that using this process, large grain

silicon ribbons can be produced with a cost as low as $13.9/M^2$ (i.e. $0.116/watt assuming 12% conversion efficiency).

REFERENCES

1. C. J. van Gurp, Semiconductor Silicon, The Electrochemical Society 1977, p. 342.
2. R. W. Bower and J. W. Mayer, Appl. Phys. Lett. 20, 359 (1972).
3. J. W. Mayer and K. N. Tu, J. Vac. Sci. Tech. 11, 86 (1974).
4. J. J. Casey, R. R. Verderber, R. R. Garnache, J. Electrochem. Soc. 114, 201, (1967).
5. A. S. Borezhnoi, Silicon and its Binary Systems, Consultants Bureau, New York, 1960, pp. 168ff.
6. ASTM Standard Powder Diffraction Patterns, Card 6-0681.
7. ASTM Standard Powder Diffraction Patterns, Card 17-415.
8. A. Joshi, L. E. Davies, P. W. Palmberg, in Methods of Surface Analysis, Vol. 1, Ed. A. W. Czanderna, Elsevier Scientific Publishing Co. (1975).
9. K. R. Sarma et al., Thin Films of Silicon on Low-Cost Substrates, Final Report, DOE Contract No. EY-76-C-03-1287. September 1978.
10. I. A. Aboaf, J. Electrochem. Soc., 114, 948 (1967).
11. C. S. Stokes, in Reactions Under Plasma Conditions, Vol. 2, Ed. M. Venugopalan, Wiley-Interscience, New York, 259 (1971).
12. C. S. Stokes, in Reactions in Electrical Discharges, Adv. in Chem. Series, ACS, 390 (1969).
13. F. C. Frank, Discussions Faraday Soc., 5, 48 (1949).
14. R. S. Wagner, W. C. Ellis, Appl. Phys. Lett., 4, 89 (1964); R. S. Wagner, W. C. Ellis, K. A. Jackson, S. M. Arnold, J. Appl. Phys., 35, 2993 (1964); R. S. Wagner and W. C. Ellis, Trans. of the Met. Soc. of AIME, 233, 1053 (1965); R. S. Wagner and C. J. Doherty, J. Elect. Chem. Soc., 113, 1300 (1966).

15. G. A. Bootsma, M. J. Gassen, J. Crystal Growth, 10, 223 (1971).

16. W. G. Pfann, Zone Melting, pp. 198 - 208, John Wiley and Sons, New York, 1958.

17. S. Mendelson, J. Appl. Phys., 36, 2525 (1965).

18. A. I. Bennet and R. L. Longini, Phys. Rev., 116, 53 (1959); D. R. Hamilton and R. G. Seidensticker, J. Appl. Phys., 31, 1165 (1960).

19. D. Chaudhari, J. Appl. Phys., 45, 5339 (1974).

20. K. R. Sarma et. al., Thin Film Polycrystalline Silicon Solar Cells, 1st Quarterly Report, December 1978, DOE Contract No.: ET-78-C-03-2207.

21. K. R. Sarma et. al., Thin Film Polycrystalline Silicon Solar Cells, 3rd Quarterly Report, June 1979, DOE Contract No.: ET-78-C-03-2207.

22. A. Goetzberger and W. Schockley, J. Appl. Phys., 31, 1821 (1960).

23. T. F. Seidel, R. L. Meek, and A. G. Cullis, J. Appl. Phys., 46, 600 (1975).

☆ U S GOVERNMENT PRINTING OFFICE: 1980-640-258/2274